
PARTICLE FILTERING AND GAUSSIAN MIXTURES - ON A LOCALIZED MIXTURE COEFFICIENTS PARTICLE FILTER (LMCPF) FOR GLOBAL NWP

A PREPRINT

Anne Rojahn^{1*}, Nora Schenk^{1,2}, Peter Jan van Leeuwen³, Roland Potthast¹

¹ *Deutscher Wetterdienst, Data Assimilation Unit, Offenbach am Main, Germany*
² *Goethe-University Frankfurt, Institute of Mathematics, Frankfurt am Main, Germany*
³ *Colorado State University, Department of Atmospheric Science, USA*

June 16, 2022

ABSTRACT

In a global numerical weather prediction (NWP) modeling framework we study the implementation of *Gaussian uncertainty* of individual particles into the assimilation step of a localized adaptive particle filter (LAPF). We obtain a local representation of the prior distribution as a mixture of basis functions. In the assimilation step, the filter calculates the individual weight coefficients and new particle locations. It can be viewed as a combination of the LAPF and a localized version of a Gaussian mixture filter, i.e., a *Localized Mixture Coefficients Particle Filter* (LMCPF).

Here, we investigate the feasibility of the LMCPF within a global operational framework and evaluate the relationship between prior and posterior distributions and observations. Our simulations are carried out in a standard pre-operational experimental set-up with the full global observing system, 52 km global resolution and 10^6 model variables. Statistics of particle movement in the assimilation step are calculated. The mixture approach is able to deal with the discrepancy between prior distributions and observation location in a real-world framework and to pull the particles towards the observations in a much better way than the pure LAPF. This shows that using Gaussian uncertainty can be an important tool to improve the analysis and forecast quality in a particle filter framework.

Keywords data assimilation · high dimensional · particle filter · non-Gaussian · numerical weather prediction

1 Introduction

Let us consider a state space \mathbb{R}^n of dimension $n \in \mathbb{N}$, an observation space \mathbb{R}^m of dimension $m \in \mathbb{N}$ and a sequence of observations $y_k \in \mathbb{R}^m$ at points in time t_k for time index $k = 1, 2, 3, \dots$. Based on a *prior* distribution $p_k^{(b)}(x)$, $x \in \mathbb{R}^n$, at time t_k , the task of *Bayesian data assimilation* is to calculate a *posterior* probability distribution $p_k^{(a)}(x)$, $x \in \mathbb{R}^n$, at time t_k . States and observations are linked by the equation

$$y_k = H(x_k^{true}) + \epsilon_k \quad (1.1)$$

with the true state vector $x_k^{true} \in \mathbb{R}^n$ at time t_k , some observation error ϵ_k and the *observation operator* $H : \mathbb{R}^n \rightarrow \mathbb{R}^m$. Usually, the prior $p_k^{(b)}$ is estimated from earlier analysis steps, from which the distribution is propagated through time to some recent analysis time t_k based on some numerical model M .

The approximation of a general prior distribution by an *ensemble of states*, also known as a set of *particles*, has a long tradition in mathematical stochastics, see for example Bain and Crisan [2009]. It is also well-known, that sampling as

*Corresponding author: Anne Rojahn, Deutscher Wetterdienst, Data Assimilation Unit, Frankfurter Strasse 135, 63067 Offenbach am Main, Germany. E-mail: anne.walter@dwd.de

usually carried out by Markov Chain Monte Carlo (MCMC) methods [Anderson and Anderson, 1999, Bain and Crisan, 2009, Crisan and Rozovski, 2011] works well in low dimensions, but when we sample in a high-dimensional space (where high usually refers to dimensions above $n=5$), the methods basically collapse, since the number of necessary samples to find some probability different from zero grows exponentially with the dimension [van Leeuwen, 2010, Snyder et al., 2008, 2015, Bickel et al., 2008]. Alternative methods based on particular approximations of the prior and posterior have been developed, with the *Ensemble Kalman Filter* (EnKF) [Evensen, 1994, Evensen and van Leeuwen, 2000, Evensen, 2009] and the *Local Ensemble Transform Kalman Filter* (LETKF) by Hunt et al. [2007] as important and widely used methods for high-dimensional filtering. These methods, however, rely on the approximation of the prior by a Gaussian, which is a strong limitation when applied to highly non-linear dynamical systems as either global or high-resolution *Numerical Weather Prediction* (NWP).

Different routes to carry out non-Gaussian assimilation have been taken by the filtering community for example with Gaussian mixtures [Anderson and Anderson, 1999], locally applied Gaussian mixtures [Bengtsson et al., 2003] or by the development of particular filters such as the GIGG filter of Bishop [2016]. For an overview of different ensemble-based data assimilation methods, we refer to Vetra-Carvalho et al. [2018] and van Leeuwen et al. [2019]. An alternative route has been chosen by the 4D-VAR community with an ensemble of 4D-VARS based on perturbed observations, compare Klinker et al. [2000].

Over the past years *particle filters* have become mature enough to be used for very-high-dimensional non-Gaussian filtering, compare van Leeuwen [2009], van Leeuwen et al. [2015], Farchi and Bocquet [2018] and van Leeuwen et al. [2019] for recent reviews. *Localization* for particle filters is used by Reich and Cotter [2015], Poterjoy and Anderson [2016], Penny and Miyoshi [2016] and Potthast et al. [2019]. Instead of the localization Kawabata and Ueno [2020] have used an adaptive observation error estimator to avoid the filter collapse in a regional mesoscale model. Particle filters have been successfully used for full-scale NWP systems. In particular, in Poterjoy et al. [2017] a localized particle filter has been studied for a regional numerical weather prediction model over the US. The team Frei and Künsch [2013] developed a *hybrid Ensemble Kalman Particle Filter* which Robert et al. [2017] has tested for the regional COSMO NWP model. The *Localized Adaptive Particle Filter* (LAPF) described in Potthast et al. [2019] has been tested for the global ICON NWP model. The LAPF [Potthast et al., 2019] has shown to provide reasonable assimilation results for an global atmospheric data assimilation for the ICON model in quasi-operational setup. It has been successfully run for a month of assimilations with 10^6 degrees of freedom (52 km global resolution) and shows a stable behaviour synchronizing the system with reality.

Here, our starting point is the investigation of the behaviour of the LAPF with respect to errors in the prior distribution $p_k^{(b)}$. By studying the statistics of the observations vector mapped into ensemble space, we will show that in many cases the model forecasts show significant distance to the observations, and the particle filter based on a limited number of delta distributions does not pull the particles close enough to the observations when the move of particles is only achieved through adaptive resampling.

To allow individual particles to move towards the observations, we further develop the LAPF by bringing ideas from Gaussian mixtures into its framework. We reach this goal by including model and forecast uncertainty for each particle, as for example suggested by the *Low-Rank Kernel Particle Kalman Filter* (LRKPKF) of Hoteit et al. [2008], compare also Liu et al. [2016a] and Liu et al. [2016b]. The basic idea is to consider each particle to be a Gaussian where its width is representing its uncertainty. This means we study a prior distribution given by a Gaussian (or more general radial basis function RBF) mixture. Then, the prior has the form

$$p^{(b)}(x) := c \sum_{\ell=1}^L c_{\ell} e^{-\frac{1}{2}(x-x^{(b,\ell)})^T \mathbf{G}^{-1}(x-x^{(b,\ell)})}, \quad x \in \mathbb{R}^n, \quad (1.2)$$

with constants $c_{\ell} = 1/\sqrt{(2\pi)^n \det(\mathbf{G})}$ for the individual Gaussian basis functions with mean $x^{(b,\ell)}$ and covariance \mathbf{G} and a normalization constant c , which in this case is given by $c = 1/L$, but is used as a generic constant which is different in different equations. For this approximation, and when the observation operator H is linear, we can explicitly calculate the posterior distribution as a corresponding Gaussian mixture, i.e.,

$$p^{(a)}(x) := c \sum_{\ell=1}^L c_{\ell} w_{\ell} e^{-\frac{1}{2}(x-\tilde{x}^{(a,\ell)})^T \tilde{\mathbf{G}}^{-1}(x-\tilde{x}^{(a,\ell)})}, \quad x \in \mathbb{R}^n, \quad (1.3)$$

with some matrix $\tilde{\mathbf{G}}$ (calculated e.g. in Chapter 5.4 of Nakamura and Potthast [2015]), constants $c_{\ell} w_{\ell}$ (not normalized at this point, since different Gaussians get different weight in this first Bayesian step) and temporary analysis states $\tilde{x}^{(a,\ell)}$, $\ell = 1, \dots, L$, with the components

$$q^{(a,\ell)}(x) := c c_{\ell} w_{\ell} e^{-\frac{1}{2}(x-\tilde{x}^{(a,\ell)})^T \tilde{\mathbf{G}}^{-1}(x-\tilde{x}^{(a,\ell)})}, \quad x \in \mathbb{R}^n. \quad (1.4)$$

The constant c will normalize the integral of $p^{(a)}$ to one. If there are no further constraints to the variables, the ℓ -th posterior particle can be directly drawn with relative probability $c_\ell w_\ell$ from the distribution component $q^{(a,\ell)}(x)$ leading to an analysis ensemble member $x^{(a,\ell)}$. This drawing process is carried out based on *localization*, *adaptivity* and the *transformation into ensemble space* as developed for the LAPF [Potthast et al., 2019]; details will be described in Sections 2.1 and 2.2. As for other particle filters, the posterior particles will be calculated by an ensemble transform matrix, with details worked out in Section 2.2. For each posterior ensemble member, based on the prior Gaussian mixture, this matrix defines *coefficients* describing the weights of each particle. The name *Local Mixture Coefficients Particle Filter (LMCPF)* has been used to distinguish from other localized particle filter methods. For example, Reich and Cotter [2015] present Localized Particle Filter (LPF) versions, which include sophisticated optimal transport properties. A further LPF method is introduced by Penny and Miyoshi [2016] and the LAPF (already implemented at the German Weather Service in 2014²) is presented by Potthast et al. [2019]. We note that the choice for \mathbf{G} of formula (1.2) as a scaled version of Hunt the ensemble correlation matrix, i.e., $\mathbf{G} = \kappa \mathbf{B}$, with $\mathbf{B} = \frac{1}{(L-1)} \mathbf{X}\mathbf{X}^T$, resembles the choices made for the LETKF [Hunt et al., 2007] and leads to very efficient code.

We will investigate the usefulness of the Gaussian uncertainty within the particle filter in very high-dimensional systems, leading to moves or shifts of the particles towards the observations. Statistics of these shifts will be shown, demonstrating that for this global atmospheric NWP system the uncertainty plays an important role. Further, our numerical results show that the LMCPF is a particle filter with a quality comparable to the LETKF for state-of-the-art real-world operational global atmospheric NWP forecasting systems. This will be demonstrated by numerical experiments based on an implementation of the particle filter in the operational data assimilation software suite DACE³ of Deutscher Wetterdienst (DWD).

The *Localized Mixture Coefficients Particle Filter* is introduced in Section 2, where we first summarize the ingredients we build on in Section 2.1. Then, an elementary Gaussian filtering step in ensemble space is described in Section 2.2. Finally, the full LMCPF method is presented in Section 2.3. We describe the high-dimensional experimental environment for our development and evaluation framework for numerical tests in Section 3. The numerical results for the global weather forecasting model ICON are shown in Section 4. We study the statistics of the relationship of observations and the ensemble as well as the corresponding statistics of the shift vectors of the Gaussian particles of the LMCPF. We show the large improvements with respect to standard NWP scores which the LMCPF can achieve compared to the LAPF. Additionally, we present case studies comparing the LMCPF forecast scores to the operational LETKF.

2 Localized Mixture Coefficients Particle Filter (LMCPF)

The basic idea of a Bayesian assimilation step is to calculate a posterior distribution $p^{(a)}(x)$ for a state $x \in \mathbb{R}^n$ based on a prior distribution $p^{(b)}(x)$ for $x \in \mathbb{R}^n$, some measurement $y \in \mathbb{R}^m$ and a distribution of the measurement error $p(y|x)$ of y given the state x . The famous Bayes formula calculates

$$p^{(a)}(x) = cp^{(b)}(x) \cdot p(y|x), \quad x \in \mathbb{R}^n, \quad (2.1)$$

with normalization constant c such that $\int_{\mathbb{R}^n} p^{(a)}(x) dx = 1$.

Our setup for data assimilation is to employ an ensemble $\{x^{(b,\ell)} \in \mathbb{R}^n, \ell = 1, \dots, L\}$ of states, which are used to estimate or approximate $p^{(b)}(x)$. The basic analysis step of data assimilation is to construct an analysis ensemble $\{x^{(a,\ell)} \in \mathbb{R}^n, \ell = 1, \dots, L\}$ of *analysis states*, which approximate $p^{(a)}(x)$ in a way consistent with the approximation of $p^{(b)}(x)$ by $x^{(b,\ell)}$, $\ell = 1, \dots, L$. The above idea is common to both the Ensemble Kalman Filter (EnKF) and to particle filters. We employ the notation

$$\mathbf{X}^{(b)} := \left(x^{(b,1)} - \bar{x}, \dots, x^{(b,L)} - \bar{x} \right) \in \mathbb{R}^{n \times L} \quad (2.2)$$

for the matrix of ensemble differences to the ensemble mean \bar{x} defined by

$$\bar{x} := \frac{1}{L} \sum_{\ell=1}^L x^{(b,\ell)} \in \mathbb{R}^n. \quad (2.3)$$

For the ensemble differences in observation space we employ

$$\mathbf{Y}^{(b)} := \left(y^{(b,1)} - \bar{y}, \dots, y^{(b,L)} - \bar{y} \right) \in \mathbb{R}^{m \times L} \quad (2.4)$$

²Shown by German Climate Computing Center DKRZ Git Records

³Data Assimilation Coding Environment

with the mean \bar{y} defined by

$$\bar{y} := \frac{1}{L} \sum_{\ell=1}^L y^{(b,\ell)} \in \mathbb{R}^m \quad (2.5)$$

and

$$y^{(b,\ell)} := H(x^{(b,\ell)}). \quad (2.6)$$

From now on we will use \mathbf{X} for $\mathbf{X}^{(b)}$ and \mathbf{Y} for $\mathbf{Y}^{(b)}$ for brevity. In the case of a linear observation operator we have $\bar{y} = \mathbf{H}\bar{x}$ and $\mathbf{Y} = \mathbf{H}\mathbf{X}$. Usually, for Ensemble Kalman Filters, the approximation of the covariance matrix is chosen to be based on the estimator

$$\mathbf{B} := \frac{1}{L-1} \sum_{\ell=1}^L (x^{(\ell)} - \bar{x}) \cdot (x^{(\ell)} - \bar{x})^T \in \mathbb{R}^{n \times n}. \quad (2.7)$$

The estimator \mathbf{B} can also be written as $\mathbf{B} = \frac{1}{L-1} \mathbf{X}\mathbf{X}^T$. Usually, in this case the prior is approximated by

$$p^{(b)}(x) = c_B e^{-\frac{1}{2}(x-\bar{x})^T \mathbf{B}^{-1}(x-\bar{x})} \quad (2.8)$$

with \mathbf{B}^{-1} well defined⁴ for all $x = \bar{x} + \mathbf{X}\beta$ with some vector $\beta \in \mathbb{R}^L$. The normalization constant c_B can be calculated based on a matrix Φ which consists of an orthonormal basis of $N(X)^\perp \subset \mathbb{R}^L$ of dimension $\tilde{L} < L$ by

$$c_B := \left(\int_{\mathbb{R}^{\tilde{L}}} e^{-\frac{1}{2}(X\Phi\alpha)^T \mathbf{B}^{-1}(X\Phi\alpha)} \sqrt{\det(\Phi^T X^T X \Phi)} d\alpha \right)^{-1}, \quad (2.9)$$

where $\det(\Phi^T X^T X \Phi)$ is the Gramian of the injective mapping $X\Phi : \mathbb{R}^{\tilde{L}} \rightarrow \mathbb{R}^n$, i.e. the determinant of the Gram matrix $\Phi^T X^T X \Phi$. The approximation of the *classical particle filter* is

$$p^{(b)}(x) = c \sum_{\ell=1}^L \delta(x - x^{(b,\ell)}), \quad x \in \mathbb{R}^n, \quad (2.10)$$

with the *delta distribution* $\delta(\cdot)$ and a normalization constant $c = 1/L$. A well-known idea is to employ *Gaussian mixtures* (c.f. Hoteit et al. [2008], Liu et al. [2016a,b]), i.e., use the approximation

$$p^{(b)}(x) = c \sum_{\ell=1}^L c_\ell e^{-\frac{1}{2}(x-x^{(b,\ell)})^T \mathbf{G}_\ell^{-1}(x-x^{(b,\ell)})}, \quad (2.11)$$

where $\mathbf{G}_\ell \in \mathbb{R}^{n \times n}$ is some symmetric and positive definite matrix which describes the *uncertainty* of the individual particle, $c_\ell = 1/\sqrt{(2\pi)^n \det(\mathbf{G}_\ell)}$ is a normalization constant for each of the Gaussians under consideration and c is an overall normalization constant.

- The matrix \mathbf{G}_ℓ is the covariance of each Gaussian and can be seen as a measure for the short-range *forecast error* consisting of model error and some of the uncertainty in the initial conditions beyond the distribution of the ensemble of particles itself. We will discuss the important role of \mathbf{G}_ℓ in several places later, when we describe the LMCPF and its numerical realization. In particular, we will investigate the situation where G is a multiple of the covariance matrix B defined above.
- The Gaussian mixture filter can be seen as a generalization of the classical particle filter, where instead of a delta distribution a Gaussian around each prior particle is employed to calculate the posterior distribution and draw from it. Here, we will employ *localization* and *adaptivity* as developed for the LAPF in combination with the mixture concept within the LMCPF.

⁴The standard arguments, see Lemma 3.2.1 of Nakamura and Potthast [2015], show injectivity of XX^T on $R(X)$: $XX^T X\beta = 0$ with $\beta \in \mathbb{R}^L$ yields $X^T X\beta \in N(X) \cap R(X^T) = R(X^T)^\perp \cap R(X^T)$, thus $X^T X\beta = 0$. The same argument for $X\beta \in N(X^T)$ yields $X\beta = 0$, thus XX^T is injective on $R(X)$. For surjectivity we consider $v \in R(X)$, i.e. $v = Xw$ with $w \in \mathbb{R}^L = N(X) \oplus N(X)^\perp = N(X) \oplus R(X^T)$, such that $w = w_1 + w_2$ with $w_1 \in N(X)$ and $w_2 = X^T \beta$ with some $\beta \in \mathbb{R}^n = R(X) + R(X)^\perp$. Repeating the last argument leads to a $\beta_1 \in R(X)$ with $w = X^T \beta_1$ and thus surjectivity. Invertibility of B is thus shown.

2.1 The Localized Adaptive Particle Filtering Ingredients and Preparations

The goal of this section is to collect, prepare and summarize all components employed for the *localized mixture coefficients particle filter*. For the following derivation we assume linearity of \mathbf{H} , we will discuss the form of the equations in the case of non-linear \mathbf{H} later. Then, we have $\mathbf{Y}^T = \mathbf{X}^T \mathbf{H}^T$ and with $\gamma = \frac{1}{L-1}$ the standard estimator for the covariance matrix is given by $\mathbf{B} = \gamma \mathbf{X} \mathbf{X}^T$. We will later use \mathbf{B} as measure of uncertainty of individual particles, then using the scaling

$$\gamma = \frac{\kappa}{(L-1)} \quad (2.12)$$

with a parameter $\kappa > 0$ scaling the standard covariance matrix. Following standard arguments as in Hunt et al. [2007], Nakamura and Potthast [2015] or Potthast et al. [2019], this leads to the *Kalman gain*

$$\begin{aligned} \mathbf{K} &= \mathbf{B} \mathbf{H}^T (\mathbf{R} + \mathbf{H} \mathbf{B} \mathbf{H}^T)^{-1} \\ &= \gamma \mathbf{X} \mathbf{X}^T \mathbf{H}^T (\mathbf{R} + \gamma \mathbf{H} \mathbf{X} \mathbf{X}^T \mathbf{H}^T)^{-1} \\ &= \gamma \mathbf{X} \mathbf{Y}^T (\mathbf{R} + \gamma \mathbf{Y} \mathbf{Y}^T)^{-1} \end{aligned} \quad (2.13)$$

with invertible observation error covariance matrix $\mathbf{R} \in \mathbb{R}^{m \times m}$. We note that we have

$$(\mathbf{I} + \gamma \mathbf{Y}^T \mathbf{R}^{-1} \mathbf{Y}) \mathbf{Y}^T = \mathbf{Y}^T \mathbf{R}^{-1} (\mathbf{R} + \gamma \mathbf{Y} \mathbf{Y}^T) \quad (2.14)$$

by elementary calculations. We also note that $\mathbf{I} + \gamma \mathbf{Y}^T \mathbf{R}^{-1} \mathbf{Y}$ is invertible on \mathbb{R}^L and $\mathbf{R} + \gamma \mathbf{Y} \mathbf{Y}^T$ is invertible on \mathbb{R}^m by assumption on the invertibility of \mathbf{R} . Then, multiplying (2.14) by $(\mathbf{I} + \gamma \mathbf{Y}^T \mathbf{R}^{-1} \mathbf{Y})^{-1}$ from the left and by $(\mathbf{R} + \gamma \mathbf{Y} \mathbf{Y}^T)^{-1}$ from the right we obtain

$$\mathbf{Y}^T (\mathbf{R} + \gamma \mathbf{Y} \mathbf{Y}^T)^{-1} = (\mathbf{I} + \gamma \mathbf{Y}^T \mathbf{R}^{-1} \mathbf{Y})^{-1} \mathbf{Y}^T \mathbf{R}^{-1}. \quad (2.15)$$

Now, (2.15) can be used to transform (2.13) into

$$\mathbf{K} = \gamma \mathbf{X} (\mathbf{I} + \gamma \mathbf{Y}^T \mathbf{R}^{-1} \mathbf{Y})^{-1} \mathbf{Y}^T \mathbf{R}^{-1}. \quad (2.16)$$

This can be used to calculate the covariance update step of the Kalman filter in ensemble space as follows. We derive

$$\begin{aligned} \mathbf{B}^{(a)} &= (\mathbf{I} - \mathbf{K} \mathbf{H}) \mathbf{B}^{(b)} \\ &= \left(\mathbf{I} - \gamma \mathbf{X} (\mathbf{I} + \gamma \mathbf{Y}^T \mathbf{R}^{-1} \mathbf{Y})^{-1} \mathbf{Y}^T \mathbf{R}^{-1} \mathbf{H} \right) \gamma \mathbf{X} \mathbf{X}^T \\ &= \mathbf{X} \left(\mathbf{I} - \gamma (\mathbf{I} + \gamma \mathbf{Y}^T \mathbf{R}^{-1} \mathbf{Y})^{-1} \mathbf{Y}^T \mathbf{R}^{-1} \mathbf{Y} \right) \gamma \mathbf{X}^T \\ &= \mathbf{X} \left((\mathbf{I} + \gamma \mathbf{Y}^T \mathbf{R}^{-1} \mathbf{Y})^{-1} \left[\mathbf{I} + \gamma \mathbf{Y}^T \mathbf{R}^{-1} \mathbf{Y} - \gamma \mathbf{Y}^T \mathbf{R}^{-1} \mathbf{Y} \right] \right) \gamma \mathbf{X}^T \\ &= \mathbf{X} (\mathbf{I} + \gamma \mathbf{Y}^T \mathbf{R}^{-1} \mathbf{Y})^{-1} \gamma \mathbf{X}^T \\ &= \gamma \mathbf{X} (\mathbf{I} + \gamma \mathbf{Y}^T \mathbf{R}^{-1} \mathbf{Y})^{-1} \mathbf{X}^T. \end{aligned} \quad (2.17)$$

The analysis ensemble $\mathbf{X}^{(a)}$ which generates the correct posterior covariance by $\mathbf{B}^{(a)} = \gamma \mathbf{X}^{(a)} (\mathbf{X}^{(a)})^T$ is given by

$$\mathbf{X}^{(a)} := \mathbf{X}^{(b)} \left(\mathbf{I} + \gamma \mathbf{Y}^T \mathbf{R}^{-1} \mathbf{Y} \right)^{-\frac{1}{2}} \in \mathbb{R}^{n \times L}, \quad (2.18)$$

where the matrix $\mathbf{I} + \gamma \mathbf{Y}^T \mathbf{R}^{-1} \mathbf{Y} \in \mathbb{R}^{L \times L}$ lives in ensemble space, it is symmetric and invertible by construction, for all $\gamma > 0$.

The localized ensemble transform Kalman filter (LETKF) following Hunt et al. [2007] based on the square root filter for calculating the analysis ensemble can be written as

$$\bar{\mathbf{x}}^{(a)} := \bar{\mathbf{x}}^{(b)} + \gamma \mathbf{X}^{(b)} w = \bar{\mathbf{x}}^{(b)} + \mathbf{K} (y - \bar{y}) \quad (2.19)$$

with

$$w := (\mathbf{I} + \gamma \mathbf{Y}^T \mathbf{R}^{-1} \mathbf{Y})^{-1} \mathbf{Y}^T \mathbf{R}^{-1} (y - \bar{y}) \in \mathbb{R}^L \quad (2.20)$$

and

$$\mathbf{X}^{(a)} := \mathbf{X}^{(b)} \mathbf{W} \quad (2.21)$$

with

$$\mathbf{W} := (\mathbf{I} + \gamma \mathbf{Y}^T \mathbf{R}^{-1} \mathbf{Y})^{-\frac{1}{2}} \in \mathbb{R}^{L \times L}. \quad (2.22)$$

The above equations are carried out at each analysis grid point where the matrix \mathbf{R} is localized by multiplication of each entry with a localization function depending on the distance of the variable to the analysis grid point Hunt et al. [2007]. Using

$$\mathbf{X}^{(a,full)} := \left(x^{(a,1)}, \dots, x^{(a,L)} \right) = (\bar{x}^{(a)} + x^{(a)}) \in \mathbb{R}^{n \times L} \quad (2.23)$$

the full update of the LETKF ensemble can be written as

$$\mathbf{X}^{(a,full)} = \bar{x}^{(b)} + \gamma \mathbf{X}^{(b)} w + \mathbf{X}^{(b)} \mathbf{W}, \quad (2.24)$$

where we define the sum of a vector (here $\bar{x}^{(b)}$ or $\gamma \mathbf{X}^{(b)} w$) plus a matrix (here $\mathbf{X}^{(b)} \mathbf{W}$) by adding the vector to each column of the matrix.

For non-linear observation operator H as in (18) of Hunt et al. [2007] the operator \mathbf{K} is defined by the last line of (2.13), see also (2.16) and the ensemble transform by (2.21) with \mathbf{W} by (2.22). This basically corresponds to an approximate linearization of H in observation space based on the differences $y^{(b,\ell)} - \bar{y}$.

2.2 An Elementary Gaussian Filtering Step in Ensemble Space

Let us consider a Bayesian assimilation step (2.1) based on the approximation of the prior $p^{(b)}(x)$ as a Gaussian mixture (2.11). We first describe the steps in general, then derive the ensemble space version of the equations. To each particle, we attribute a distribution with covariance \mathbf{G} , i.e., we define

$$p^{(b,\ell)}(x) := \frac{1}{\sqrt{(2\pi)^n \det(\mathbf{G})}} e^{-\frac{1}{2}(x-x^{(b,\ell)})^T \mathbf{G}^{-1}(x-x^{(b,\ell)})}, \quad x \in \mathbb{R}^n, \quad (2.25)$$

which is normalized according to equation (4.5.28) of Nakamura and Potthast [2015]. Then, the full prior is a *Gaussian mixture*

$$p^{(b)}(x) = c \sum_{\ell=1}^L c_\ell e^{-\frac{1}{2}(x-x^{(b,\ell)})^T \mathbf{G}^{-1}(x-x^{(b,\ell)})}, \quad x \in \mathbb{R}^n, \quad (2.26)$$

with $c_\ell := 1/\sqrt{(2\pi)^n \det(\mathbf{G})}$ (i.e., we choose the variance uniform for all ℓ) and with some normalization constant $c = \frac{1}{L}$ in this case. Bayes formula leads to the posterior distribution

$$p^{(a)}(x) = c \sum_{\ell=1}^L c_\ell \left(e^{-\frac{1}{2}(x-x^{(b,\ell)})^T \mathbf{G}^{-1}(x-x^{(b,\ell)})} e^{-\frac{1}{2}(y-H(x))^T \mathbf{R}^{-1}(y-H(x))} \right), \quad (2.27)$$

$x \in \mathbb{R}^n$, with a normalization constant c , here different from the normalization constant in (2.26). We note that the terms in round brackets constitute individual Gaussian assimilation steps. The posterior of each of these terms can be explicitly calculated the same way as for the Ensemble Kalman Filter. Following Nakamura and Potthast [2015], Section 5.4, we define

$$x^{(a,\ell)} := x^{(b,\ell)} + \mathbf{G}\mathbf{H}^T (\mathbf{R} + \mathbf{H}\mathbf{G}\mathbf{H}^T)^{-1} (y - H(x^{(b,\ell)})), \quad \ell = 1, \dots, L, \quad (2.28)$$

and

$$\mathbf{K} = \mathbf{G}\mathbf{H}^T (\mathbf{R} + \mathbf{H}\mathbf{G}\mathbf{H}^T)^{-1}, \quad \mathbf{G}^{(a)} := (\mathbf{I} - \mathbf{K}\mathbf{H})\mathbf{G}. \quad (2.29)$$

Then, we know that

$$\begin{aligned} q^{(a,\ell)}(x) &:= c_\ell e^{-\frac{1}{2}(x-x^{(b,\ell)})^T \mathbf{G}^{-1}(x-x^{(b,\ell)})} e^{-\frac{1}{2}(y-H(x))^T \mathbf{R}^{-1}(y-H(x))} \\ &= w_\ell e^{-\frac{1}{2}(x-x^{(a,\ell)})^T [\mathbf{G}^{(a)}]^{-1}(x-x^{(a,\ell)})}, \quad x \in \mathbb{R}^n, \end{aligned} \quad (2.30)$$

with constants w_ℓ given by

$$\begin{aligned} w_\ell &= \int_{\mathbb{R}^n} c_\ell e^{-\frac{1}{2}(x-x^{(b,\ell)})^T \mathbf{G}^{-1}(x-x^{(b,\ell)})} e^{-\frac{1}{2}(y-H(x))^T \mathbf{R}^{-1}(y-H(x))} dx \\ &\quad \cdot \frac{1}{\sqrt{(2\pi)^n \det(\mathbf{G}^{(a)})}}. \end{aligned} \quad (2.31)$$

Since both c_ℓ and $\sqrt{(2\pi)^n \det(\mathbf{G}^{(a)})}$ do not depend on ℓ , the constants are irrelevant for the resampling step and will be removed by the normalization step. Note that the constants w_ℓ , $\ell = 1, \dots, L$, are extremely important, since they

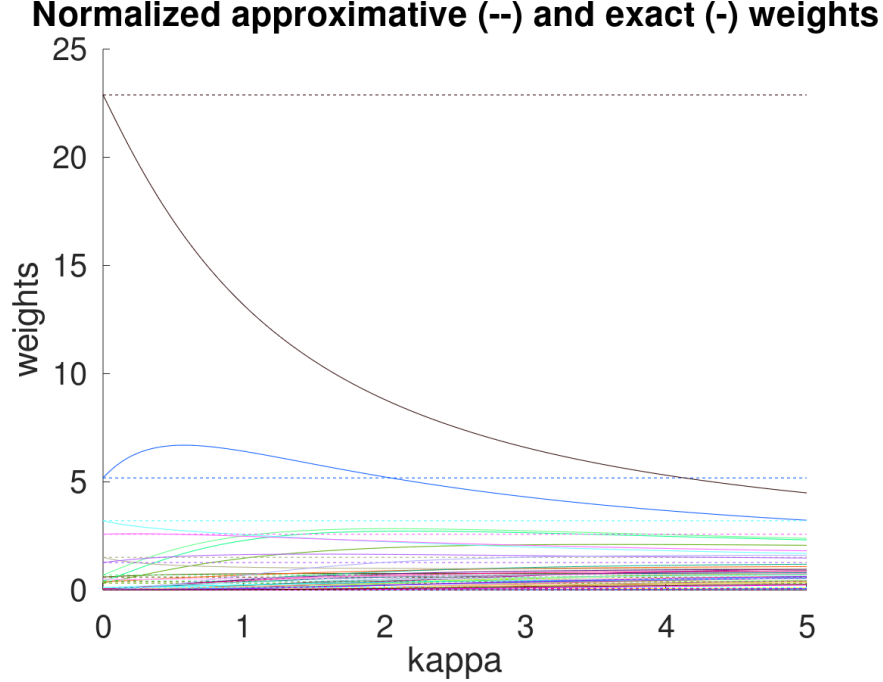


Figure 1: We show a comparison between the normalized approximative weights calculated as in (2.33) versus the normalized exact calculated weights (2.31). The solid lines show the normalized exact determined weights and the dashed lines the normalized approximative weights. The colors vary for different ensemble members ($L=40$). On the x-axis we show the value for κ of equation (2.12), on the y-axis the values of the weights.

contain the relative weights of the individual posterior particles with respect to each other. They should not be ignored! Here, we first describe the full posterior distribution, which is now given by

$$p^{(a)}(x) = c \sum_{\ell=1}^L w_{\ell} e^{-\frac{1}{2}(x-x^{(a,\ell)})^T [\mathbf{G}^{(a)}]^{-1} (x-x^{(a,\ell)})}, \quad x \in \mathbb{R}^n. \quad (2.32)$$

In the case of the classical particle filter, the Gaussians $c_{\ell} e^{-\frac{1}{2}(x-x^{(b,\ell)})^T \mathbf{G}^{-1} (x-x^{(b,\ell)})}$ become δ -distributions $c_{\ell} \delta(x - x^{(b,\ell)})$ with weights $c_{\ell} = 1$. In this case, the individual posterior weights w_{ℓ} are given by the likelihood of observations

$$w_{\ell} := e^{-\frac{1}{2}(y-H(x^{(b,\ell)}))^T \mathbf{R}^{-1} (y-H(x^{(b,\ell)}))}, \quad \ell = 1, \dots, L. \quad (2.33)$$

This choice will also be a reasonable approximation in the case of small variance \mathbf{G} of the Gaussians under consideration in comparison with the distance $y - H(x^{(b,\ell)})$. In the general Gaussian case, the weights can be calculated from (2.31). For our numerical experiments we use G non-zero with some positive variance, but approximate w_{ℓ} by (2.33).

In Figure 1 we show a comparison of the normalized approximative weights (2.33) as dashed lines and the normalized exact determined weights (2.31) as solid lines, for a selected point of the full NWP model described in Sections 3 and 4. Here, each ensemble member ($L=40$) is described by a different color. For this plot we varied the parameter κ , described in equation (2.12), between 0 and 5. Figure 1 shows how the normalized approximative weights differ from the normalized exact weights. The assumptions used to carry out our experiments may not be fully justified. Clearly, further study and experimental work is necessary.

Let us now describe the ensemble space transformation of the above equations. The ensemble space as a subset of the state space is spanned by \mathbf{X} given in (2.2). Our *ansatz* for the *model error* covariance is $\gamma \mathbf{X} \mathbf{X}^T$ with some scaling factor γ . We note that for the LETKF, $\gamma = \frac{1}{L-1}$. Here, $\gamma > 0$ can be any real number. We will provide some estimates for what γ can be in a global NWP model setup in our numerical part in Section 4. In the transformed space this leads to the covariance $\gamma \mathbf{I} \in \mathbb{R}^{L \times L}$ to be used for the ensemble transform version of (2.27). Recall the ensemble transformation $x - \bar{x} = \mathbf{X} \beta$, $x^{(\ell)} - \bar{x} = \mathbf{X} e_{\ell}$ and $x - x^{(\ell)} = \mathbf{X}(\beta - e_{\ell})$ for $\ell = 1, \dots, L$, where e_{ℓ} is the standard unit vector with

one in its ℓ -th component and zero otherwise leading to

$$\begin{aligned} (x - x^{(\ell)})^T (\gamma \mathbf{X} \mathbf{X}^T)^{-1} (x - x^{(\ell)}) &= (\beta - e_\ell)^T \gamma^{-1} \mathbf{X}^T (\mathbf{X} \mathbf{X}^T)^{-1} \mathbf{X} (\beta - e_\ell) \\ &= (\beta - e_\ell)^T \gamma^{-1} \mathbf{I} (\beta - e_\ell). \end{aligned} \quad (2.34)$$

We note that $\mathbf{X}^T (\mathbf{X} \mathbf{X}^T)^{-1} \mathbf{X} = \mathbf{I}$ is true only on the subspace $N(\mathbf{X})^\perp$, but we can employ the arguments used to justify equation (15) of Hunt et al. [2007] to use the covariance $\gamma^{-1} \mathbf{I}$ in ensemble space for the prior term. For the observation error term of (2.27) in ensemble space \mathbb{R}^L we use equation (11) of Potthast et al. [2019], i.e., we have

$$q^{(a,\ell)}(\beta) = c_\ell e^{-\frac{1}{2}(\beta - e_\ell)^T (\gamma^{-1} \mathbf{I}) (\beta - e_\ell)} e^{-\frac{1}{2}[P(y - \bar{y} - \mathbf{Y}\beta)]^T \mathbf{R}^{-1} [P(y - \bar{y} - \mathbf{Y}\beta)]}, \quad \beta \in \mathbb{R}^L, \quad (2.35)$$

for $\ell = 1, \dots, L$, where P is the orthogonal projection onto $\text{span}\{\mathbf{Y}\}$ with respect to the scalar product in \mathbb{R}^m weighted by \mathbf{R}^{-1} ; it is defined in equation (10) of Potthast et al. [2019] and Lemma 3.2.3 of Nakamura and Potthast [2015] to be given by

$$P = \mathbf{Y} (\mathbf{Y}^T \mathbf{R}^{-1} \mathbf{Y})^{-1} \mathbf{Y}^T \mathbf{R}^{-1}. \quad (2.36)$$

As in (13) - (15) of Potthast et al. [2019] the right-hand side of (2.35) can be transformed into

$$q^{(a,\ell)}(\beta) = e^{-\frac{1}{2}(\beta - e_\ell)^T (\gamma^{-1} \mathbf{I}) (\beta - e_\ell)} e^{-\frac{1}{2}[C - \beta]^T \mathbf{A} [C - \beta]}, \quad \ell = 1, \dots, L, \quad (2.37)$$

with

$$\mathbf{A} := \mathbf{Y}^T \mathbf{R}^{-1} \mathbf{Y}, \quad C := \mathbf{A}^{-1} \mathbf{Y}^T \mathbf{R}^{-1} (y - \bar{y}). \quad (2.38)$$

We now carry out (2.28) and (2.29) in ensemble space based on (2.13) and (2.14), leading to the new mean of the posterior distribution for the ℓ -th particle prior distribution

$$\beta^{(a,\ell)} = e_\ell + \gamma (\mathbf{I} + \gamma \mathbf{Y}^T \mathbf{R}^{-1} \mathbf{Y})^{-1} \mathbf{Y}^T \mathbf{R}^{-1} \mathbf{Y} (C - e_\ell) \quad (2.39)$$

and the new covariance matrix of this distribution

$$\mathbf{G}_{ens}^{(a)} = \left(\frac{1}{\gamma} \mathbf{I} + \mathbf{Y}^T \mathbf{R}^{-1} \mathbf{Y} \right)^{-1} \in \mathbb{R}^{L \times L} \quad (2.40)$$

independent of ℓ when $\mathbf{G} = \gamma \mathbf{X} \mathbf{X}^T$ is independent of ℓ . This means that we obtain

$$q^{(a,\ell)}(\beta) = w_\ell e^{-\frac{1}{2}(\beta - \beta^{(a,\ell)})^T \mathbf{G}_{ens}^{(a)} (\beta - \beta^{(a,\ell)})}, \quad \beta \in \mathbb{R}^L \quad (2.41)$$

with $\beta^{(a,\ell)}$ given by (2.39) and $\mathbf{G}_{ens}^{(a)}$ given by (2.40) for the *posterior distribution* of the ℓ -th particle in ensemble space. We denote the term

$$\beta^{(shift,\ell)} := \gamma (\mathbf{I} + \gamma \mathbf{Y}^T \mathbf{R}^{-1} \mathbf{Y})^{-1} \mathbf{Y}^T \mathbf{R}^{-1} \mathbf{Y} (C - e_\ell) \quad (2.42)$$

as the *shift vector* for the ℓ -th particle in ensemble space, i.e., $\beta^{(a,\ell)} = e_\ell + \beta^{(shift,\ell)}$ in Eq. 2.39. The use of the model error $\gamma \mathbf{I}$ corresponding to $\gamma \mathbf{X} \mathbf{X}^T$ for this particle in ensemble space leads to this shift in the analysis. The shift has important effects:

1. it moves the particle towards the observation in ensemble space,
2. by the use of particle uncertainty, it constitutes a further degree of freedom which can be used for tuning of a real system.

One of the major advantages and problems at the same time of the LAPF as well as a classical particle filter is that the particles are taken as they are. If the model has some local bias, i.e., if all particles have a similar behaviour and do not fit the observation well, then there is no inherent tool in the classical particle filter or the basic LAPF to move the particles towards the observation - this move is only achieved by selection of the best particles, closest to the observation. By resampling and rejuvenation, effectively the whole ensemble is moved towards the observation. Here, with the introduction of uncertainty of individual particles into the assimilation step, this is already carried out for each individual particle by calculating a posterior mean $\beta^{(a,\ell)}$ in (2.39) of the posterior component $q^{(a,\ell)}(\beta)$ given by (2.41) for the model error prior distribution $q^{(b,\ell)}(x)$ attributed to each particle (2.25).

2.3 Putting it all together: the full LMCPF

Here, we now collect all steps to describe the full LMCPF assimilation step and data assimilation cycle. The LMCPF assimilation cycle is run analogously to the LETKF or LAPF assimilation cycle, i.e., we start with some initial ensemble $x_0^{(a,\ell)}$ at time t_0 . Then, for time steps t_k , $k = 1, 2, 3, \dots$ we

- (1) carry out a *propagation step*, i.e., we run the model forward from time t_{k-1} to t_k for each ensemble member, leading to the background ensemble $x_k^{(b,\ell)}$ at time t_k .
- (2) Then, at each localization point ξ on a coarser analysis grid \mathcal{G} we carry out the localized ensemble transform (2.38), calculating \mathbf{C} and \mathbf{A} . Localization is carried out as for the LETKF and LAPF, i.e., the matrix \mathbf{R} is weighted depending of the distance of each of its observations to the analysis point.
- (3) We now carry out a classical resampling step following Section 3.d of Potthast et al. [2019]. This leads to a matrix

$$\check{\mathbf{W}}_{i,\ell} = \begin{cases} 1, & \text{if } R_\ell \in (w_{ac_{i-1}}, w_{ac_i}], \\ 0, & \text{otherwise,} \end{cases} \quad (2.43)$$

$i, \ell = 1, \dots, L$, draw $r_\ell \sim U([0, 1])$, set $R_\ell = \ell - 1 + r_\ell$, with accumulated weights w_{ac} , $w_{ac_0} = 0$, $w_{ac_i} = w_{ac_{i-1}} + w_{k,i}$ and $\check{\mathbf{W}} \in \mathbb{R}^{L \times L}$ defined by (2.43) with entries one or zero reflecting the choice of particles. As for the LETKF and LAPF this is carried out for each localisation point ξ on a coarser analysis grid \mathcal{G} to ensure that the weight matrices only change on scales on the order of the localization length scale. Here, we use $\check{\mathbf{W}}$ instead of $\mathbf{W}(\xi)$ for brevity.

- (4) The posterior matrix $\mathbf{G}_{ens}^{(a)}$ given by (2.40) and the shift vectors $\beta^{(shift,\ell)}$ given by (2.42) for $\ell = 1, \dots, L$ are calculated for each localization point ξ . We define

$$\mathbf{W}^{(shift)} := \left(\beta^{(shift,1)}, \dots, \beta^{(shift,L)} \right) \in \mathbb{R}^{L \times L}. \quad (2.44)$$

Then, if we want the shift given by the ℓ th-particle, we obtain it by the product $\mathbf{W}^{(shift)} e_\ell$. If we have a selection matrix $\check{\mathbf{W}}$ for which each column with index ζ , $\zeta = 1, \dots, L$, contains some particle e_ℓ with $\ell = \ell(\zeta)$, which has been chosen to be the basis for the corresponding new particle, we obtain the shifts for these particles by the product $\mathbf{W}^{(shift)} \check{\mathbf{W}}$. According to the analysis equation (2.39) the new coordinates in ensemble space are calculated by

$$\left(\beta^{(a,1)}, \dots, \beta^{(a,L)} \right) = \check{\mathbf{W}} + \mathbf{W}^{(shift)} \check{\mathbf{W}}. \quad (2.45)$$

- (5) For each particle we now carry out an *adaptive Gaussian resampling or rejuvenation* step. The rejuvenation is carried out the same way as described in Section 3.e and 3.f of Potthast et al. [2019], i.e., we first calculate

$$\rho = \frac{\mathbf{d}_{o-b}^T \mathbf{d}_{o-b} - Tr(\mathbf{R})}{Tr(\mathbf{H} \frac{1}{L-1} \mathbf{X} \mathbf{X}^T \mathbf{H}^T)} \quad (2.46)$$

at each localization point, with the actual ensemble covariance matrix $\frac{1}{L-1} \mathbf{X} \mathbf{X}^T$ and with the observation minus background statistics $\mathbf{d}_{o-b} = y_k - \bar{y}_k$ where \bar{y}_k denotes the ensemble mean in observation space described in (2.5) at time t_k . Then we scale ρ by some function

$$\sigma(\rho) := \begin{cases} c_0, & \rho < \rho^{(0)}, \\ c_0 + (c_1 - c_0) \frac{\rho - \rho^{(0)}}{\rho^{(1)} - \rho^{(0)}}, & \rho^{(0)} \leq \rho \leq \rho^{(1)}, \\ c_1, & \rho > \rho^{(1)}, \end{cases} \quad (2.47)$$

where the constants $\rho^{(0)}, \rho^{(1)}, c_0, c_1$ are tuning constants. We note that temporal smoothing is applied to ρ as usual for LETKF or LAPF. Let $\mathbf{N} \in \mathbb{R}^{L \times L}$ be a matrix with entries drawn from a normal distribution, i.e., each entry is taken from a Gaussian distribution with mean zero and variance 1. This is chosen uniformly for all localization points ξ on the analysis grid \mathcal{G} . Then, the rejuvenation plus shift step is carried out by

$$\mathbf{W} := \check{\mathbf{W}} + \mathbf{W}^{(shift)} \check{\mathbf{W}} + [\mathbf{G}_{ens}^{(a)}]^{1/2} \mathbf{N} \sigma. \quad (2.48)$$

Again, we note that $\mathbf{W} = \mathbf{W}(\xi)$, $\mathbf{W}^{(shift)} = \mathbf{W}^{(shift)}(\xi)$, $\check{\mathbf{W}} = \check{\mathbf{W}}(\xi)$, $[\mathbf{G}_{ens}^{(a)}]^{1/2} = [\mathbf{G}_{ens}^{(a)}]^{1/2}(\xi)$ and $\sigma = \sigma(\xi)$ are functions of physical space with $\xi \in \mathcal{G}$ chosen from the analysis grid \mathcal{G} .

- (6) The matrices \mathbf{W} are calculated at each analysis point ξ on a coarser global analysis grid \mathcal{G} . We now interpolate the matrices onto the full model grid \mathcal{G}_{model} .
- (7) Finally we calculate the *analysis ensemble* (2.23) by

$$\begin{aligned} \mathbf{X}^{(a,full)} &= \bar{x}^{(b)} + \mathbf{X}^{(b)} \mathbf{W} \\ &= \bar{x}^{(b)} + \underbrace{\mathbf{X}^{(b)} \check{\mathbf{W}}}_{\text{class. resampling}} + \underbrace{\mathbf{X}^{(b)} \mathbf{W}^{(shift)} \check{\mathbf{W}}}_{\text{shift}} + \underbrace{\mathbf{X}^{(b)} [\mathbf{G}_{ens}^{(a)}]^{1/2} \mathbf{N} \sigma}_{\text{adapt. Gauss. resampling}} \end{aligned} \quad (2.49)$$

Comparing (2.49) with (2.24) we observe some similarities and some differences. The LETKF does not know the selection reflected by the matrix $\check{\mathbf{W}}$, instead it transforms the ensemble by its matrix \mathbf{W} . Both know a shift term, for the LETKF it is given by w , for the LMCPF by $\mathbf{W}^{(shift)}\check{\mathbf{W}}$, shifting each particle according to model error (here taken proportional to ensemble spread), where the LETKF shifts according to the full ensemble spread. The LMCPF also takes into account that part of the ensemble spread which is kept during the selection process. Further, it employs adaptive resampling around each remaining shifted particle. This helps to keep the filter stable and achieve an appropriate uncertainty described by $o - b$ statistics.

3 Experimental Environment: the Global ICON Model

3.1 The ICON Model

We have carried out experiments testing the LMCPF algorithm in the global ICON (ICOsahedral Nonhydrostatic) model, i.e., the operational global NWP model of DWD, compare Zängl et al. [2014] and Potthast et al. [2019] for further details on the systems. ICON is based on an unstructured grid of triangles generated by subdivision from an initial icosahedron. The operational resolution is 13 km for the deterministic run and 40 km for the ensembles both for the data assimilation cycle and the ensemble prediction system (EPS). The upper air prognostic variables such as wind, humidity, cloud water, cloud ice, temperature, snow and precipitation live on 90 terrain-following vertical model levels from the surface up to 75 km height. In the operational setup, we have 265 million grid points. We also note that there are further prognostic variables on the surface and on seven soil levels, in particular soil temperature and soil water content, as well as snow variables, sea ice fraction, ice thickness and ice surface temperature of ICON's integrated sea-ice model.

The data assimilation for the operational ensemble is carried out by an LETKF based on Hunt et al. [2007]. We run a data assimilation cycle with an analysis every 3 hours. Forecasts are calculated based on the analysis for 00 and 12 UTC, with 180 hours forecast lead time. For the operational system, forecasts with shorter lead times of 120 hours for 06 and 18 UTC and 30 hours for 03, 09, 15 and 21 UTC are calculated. The ensemble data assimilation cycle is run with $L=40$ members.

For the experimental setup of our study, we employ a slightly lower horizontal resolution of 52 km for the ensemble and 26 km for the deterministic run (in the operational setup a part of the observations quality control is carried out within the framework of the deterministic run, we keep this feature for our particle filter experiments). An incremental analysis update with a window of $t \in [-90 \text{ min}, 90 \text{ min}]$ around the analysis time for starting the model runs is used. The analysis is carried out for temperature, humidity and two horizontal wind components, i.e., for *four prognostic variables* per grid point. This leads to $n = 6.6 \cdot 10^6$ free variables at each ensemble data assimilation step. Forecasts are only carried out for 00 and 12 UTC. We employ $L=40$ members for the experimental runs as well.

3.2 Comparison in an Operational Framework

For testing and developing algorithms in the operational framework, the tuning of basic algorithmic constants is a crucial part. The task of testing in a real-world operational setup is much more intricate than for what is usually done when algorithms are compared in a simulation-only small-scale environment. In particular for new algorithms, the whole *model plus assimilation cycled NWP system* needs a retuning and it is difficult to compare one algorithmic layer only within a very complex system with respect to its performance. To compare two algorithms A and B, there are two important points to be taken into account:

- (1) **Tuning Status of the Methods.** There might be a *raw* or *default* version of the algorithms, but when you compare scores with the task of showing that some algorithm is better than the other, you need to compare *tuned algorithms*. In principle, you have to tune algorithm A to give the best results and then you have to tune algorithm B to give the best results and then compare the results of tuned A and tuned B. If A has been tuned for several years, but B is raw, the results give you insight into the tuning status of A and B, but not necessarily of the algorithms as such! So we have to be very careful with generic conclusions.
- (2) **Quality Control of Observations.** When you compare two algorithms for assimilation or two models, *verification* provides a variety of scores. But verification with real data needs *quality control* of these data, since otherwise scores are mainly determined by outliers, and one broken device can make the whole verification result completely useless. But how is the data quality controlled? Usually we employ $o - f$ (observation minus first guess) statistic and remove observations which are far away from the model first guess. This leads to an important point: each algorithm A and B needs to use its own quality control. If model biases change between A and B, you will have a different selection of 'good' observations.

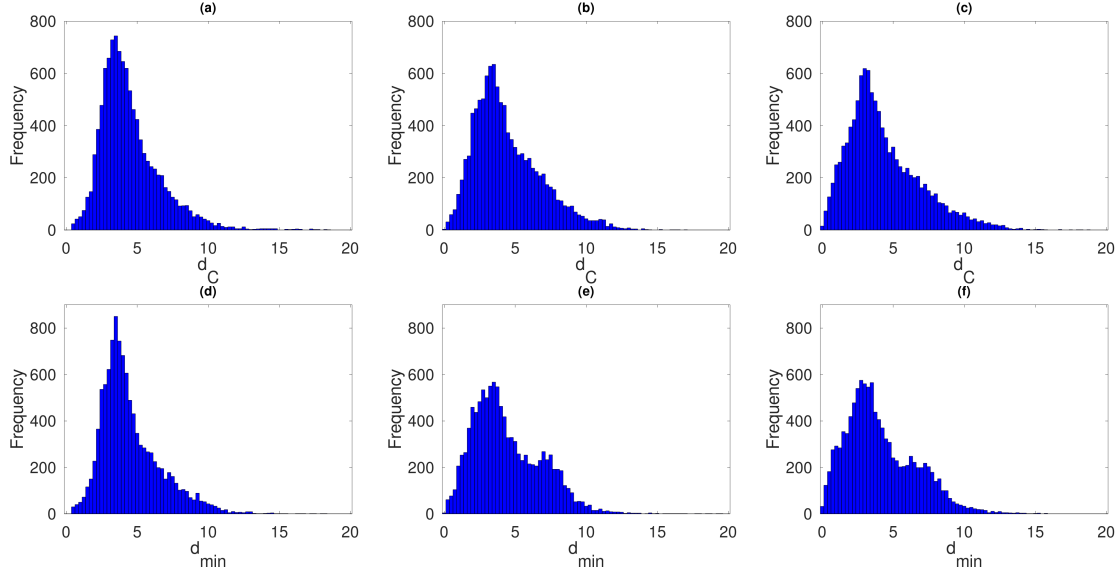


Figure 2: We show global histograms of d_C and d_{min} defined in (4.2) and (4.3) for three different pressure levels: 500 hPa in (a) and (d), 850 hPa in (b) and (e) and 1000 hPa in (c) and (f), with d_C in (a)-(c) and d_{min} in (d)-(f). Shown are statistics for the LMCPF with $\kappa = 25$ for May 6th, 0 UTC.

But how do you compare two systems which employ different observations? One solution can be to use observations for comparison which passed both quality controls. A second method is to verify each algorithm separately and then compare the scores (this is what is done with World Meteorological Organization (WMO) score comparisons between global models). A third method is to try to use 'independent' observations. But these also need some quality control, and since they are not linked to any of the forecasting systems, it is unclear in what way their use in verification helps to judge a particular algorithm or to compare two algorithms.

For our experiments, we compare the LMCPF with the LAPF and the LETKF. The LETKF has a relatively advanced tuning status. LAPF has been mildly tuned and the LMCPF is relatively new. We carried out several tuning steps to try to make LMCPF and LETKF comparable. Further, we employ quality control for the observations in each system separately. Verification of the $o - f$ statistics is based on each system independently. Here, one important performance measure is the number of observations which passes the quality control. If these number is larger for B than for A, we can conclude that the system fits better to the observations, which is a good indicator for the quality of a short-range forecast. For comparison of forecasts the joint set of observations is used, those which pass both the quality control of algorithm A and algorithm B.

4 Numerical Results

The goal of this numerical part is, *firstly*, to investigate the relationship between the observation vector mapped into ensemble space and the ensemble distribution. *Secondly*, we show since the LMCPF moves particles based on the Gaussian uncertainty of individual particles, it bridges the gap between forecast ensemble and observations. Furthermore we study its distribution. The *third* part shows results of *observation - first guess (o-f)* statistics for the LMCPF with different choices for $\kappa > 0$ compared to the LETKF and the LAPF. *Fourthly*, we investigate the evolution of ensemble spread with different parameter settings. In the last part we demonstrate the feasibility of the LMCPF as a method for atmospheric analysis and subsequent forecasting in a very high-dimensional operational framework, demonstrating that it stably runs for a month of global atmospheric analysis and forecasting.

4.1 Distributions of Observations in Ensemble Space

In a first step, we study (a) the distance between the observation and the ensemble mean and (b) the minimum distance between the observation and the ensemble members. In ensemble space, for distance calculations an appropriate metric needs to be used. Recall that \mathbb{R}^m with dimension m is the observation space and \mathbb{R}^L with dimension L the ensemble space. Given a vector $\beta \in \mathbb{R}^L$ in ensemble space, the distance corresponding to the physical norm $\|\cdot\|_{R^{-1}}$ in

observation space, which is relevant to the weight calculation of the particle filter, is calculated by

$$\begin{aligned}
\|\mathbf{Y}\beta\|_{\mathbf{R}^{-1}}^2 &= \langle \mathbf{Y}\beta, \mathbf{Y}\beta \rangle_{\mathbf{R}^{-1}} \\
&= \langle \mathbf{Y}\beta, \mathbf{R}^{-1}\mathbf{Y}\beta \rangle \\
&= (\mathbf{Y}\beta)^T \mathbf{R}^{-1} \mathbf{Y}\beta \\
&= \beta^T (\mathbf{Y}^T \mathbf{R}^{-1} \mathbf{Y}) \beta \\
&= \langle \beta, \mathbf{A}\beta \rangle \\
&= \|\beta\|_{\mathbf{A}}^2
\end{aligned} \tag{4.1}$$

where $\langle \cdot, \cdot \rangle$ denotes the standard L^2 -scalar product in \mathbb{R}^m or \mathbb{R}^L , respectively. The notation $\langle \cdot, \cdot \rangle_{\mathbf{D}}$ with some positive definite matrix \mathbf{D} denotes the weighted scalar product $\langle \cdot, \mathbf{D} \cdot \rangle$ and $\|\cdot\|_{\mathbf{D}} = \langle \cdot, \cdot \rangle_{\mathbf{D}}$, here with either \mathbf{R}^{-1} in \mathbb{R}^m or \mathbf{A} in \mathbb{R}^L . Note that for A to be positive definite we need $L \leq m$.

The matrix \mathbf{A} including the standard LETKF localization in observation space has been integrated into the data assimilation coding environment. Here, we show results from an LMCPF one month experiment studying one assimilation step at 0 UTC of May 6, 2016. The cycle has been started May 1, such that the results illustrate a situation where the spin-up period is over and LMCPF spread has reached a steady state (compare Figure 8).

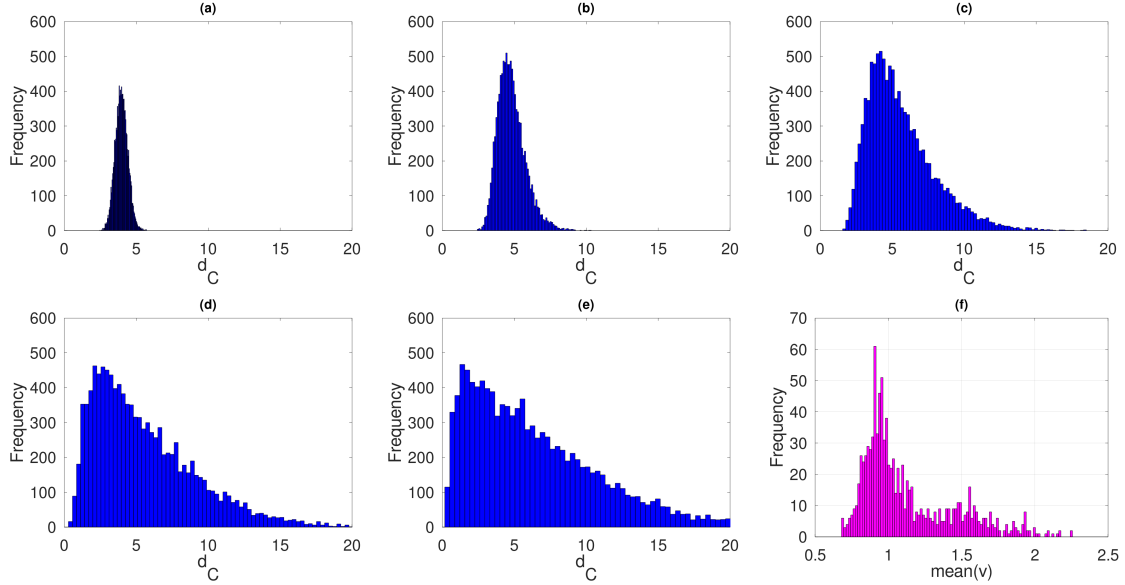


Figure 3: We show simulations of distributions of random draws in an $L = 40$ dimensional space, with different mixtures of variances given by formula (4.4), here with $\eta \in (4, 15, 30, 40, 50)$ and $\nu \in (0, 0.5, 1, 2, 3)$ in (a) to (e). A histogram of the fit of exponents ν as in (4.4) to the eigenvalue decay of the matrices \mathbf{A} for a selection of 1000 points is shown in (f). The fit is obtained from the mean of exponents derived from formula (4.5).

At each analysis grid point ξ of some coarse global analysis grid \mathcal{G} we have a matrix \mathbf{A} (see Eq. (2.38)), $L = 40$ ensemble members and one projected observation vector $C \in \mathbb{R}^L$ (see Eq. (2.38)). This leads to a total of $N_\omega = 10890$ samples ω numbering the analysis grid points in a given height layer, e.g. for 850 hPa. The distance of the observations to the ensemble mean is given by

$$d_C(\omega) := \|C(\omega)\|_{\mathbf{A}(\omega)}, \tag{4.2}$$

where the metric A is chosen to be consistent with (2.37). The minimal distance of the observations vector to the ensemble members is given by

$$d_{min}(\omega) := \min_{j=1, \dots, L} \|C(\omega) - e_j\|_{\mathbf{A}(\omega)}, \tag{4.3}$$

with $\omega = 1, \dots, N_\omega$, where we employed (4.1) and where we note that in ensemble space the ensemble members $x^{(b,j)} - \bar{x}$ are given by the standard unit normal vectors e_j , $j = 1, \dots, L$.

To analyse the role of moving particles towards the observation in ensemble space, in Figure 2 we show global histograms for d_C and d_{min} for three height levels of approximately 500 hPa, 850 hPa and 1000 hPa. When the distributions of both d_C and d_{min} are similar, i.e. the distribution of the minimal distance of the observation to the

ensemble members and the distribution of the distance of observations to the ensemble mean are comparable, it indicates that we have a well-balanced system. To understand the particular form of the distributions, we compare it with simulations of random draws of a Gaussian distribution in a 40 dimensional space shown in Figure 3. When you draw from a Gaussian with mean zero and standard deviation $\sigma = 4$, we obtain Figure 3 (a). The behaviour of the histograms of the norms of the points drawn changes significantly if we consider mixtures with different variances in different space directions. Figure 3 (a)-(e) shows different distributions with variances given by

$$\sigma_j = \frac{\eta}{j^\nu}, \quad j = 1, \dots, L \quad (4.4)$$

where the constant $\eta \in (4, 15, 30, 40, 50)$ has been chosen to achieve a maximum around 4 and different decay exponents $\nu \in (0, 0.5, 1, 2, 3)$ have been tested. The distributions of Figure 2 correspond to a decay exponent between $\nu = 1$ and $\nu = 2$. How much is this reflected by the eigenvalue distributions for the matrices \mathbf{A} ? We have carried out a fit to the eigenvalue decay of \mathbf{A} for a selection of analysis points. The constant η is obtained by using $j = 1$, which leads to $\sigma_1 = \eta$. Taking the logarithm on both sides now yields

$$\nu \log(j) = \log(\eta) - \log(\sigma_j), \quad j = 2, \dots, L. \quad (4.5)$$

A fit of ν can be obtained for example by division through $\log(j)$ and taking the mean of the remaining right-hand side. The distribution of the resulting exponents is displayed in Figure 3 (f). The results find exponents between 0.7 and 2.2. The corresponding distributions are those shown in Figure 3(c) and (d), which are quite close to the distributions of d_C found in the empirical particle-filter generated NWP ensemble Figure 2.

4.2 The Move of Particles

In a second step, we want to investigate the capability of the LMCPF to move particles towards the observation by testing different choices of $\kappa > 0$ given by (2.12). In Figure 4 we compare histograms of the norm of the mean ensemble shift in ensemble space for pressure level 500 hPa, determined for May 6th, 0 UTC. The four histograms show the statistics for the three filters in different settings: a) LAPF, b) LMCPF with $\kappa = 1$, c) LMCPF with $\kappa = 2.5$ and d) LMCPF with $\kappa = 25$.

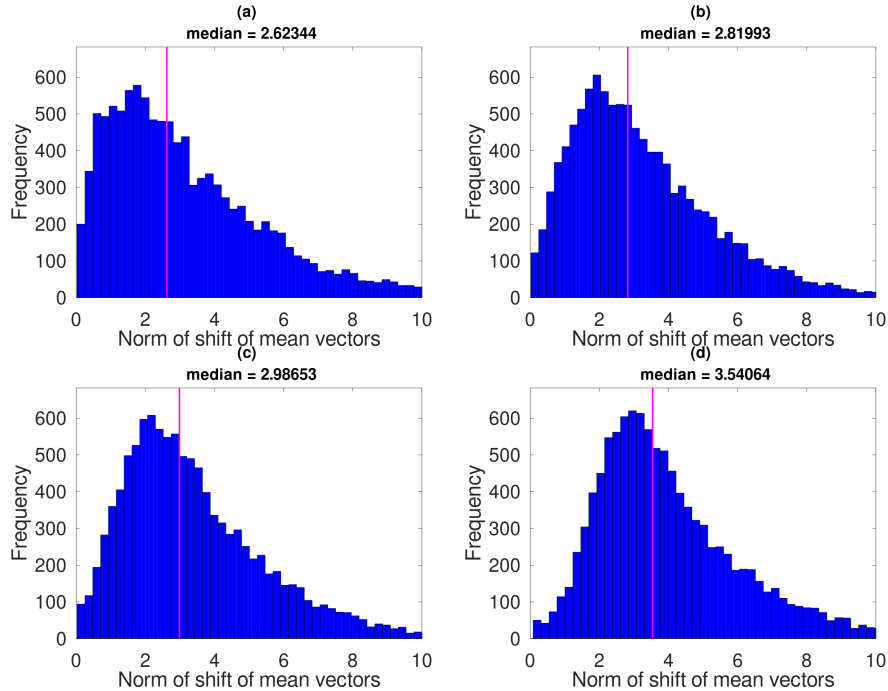


Figure 4: We show global histograms of the norm of the mean ensemble shift at pressure level at 500hPa. On the x-axis we show the norm of shift of mean vectors in ensemble space and on the y-axis we show the frequency. We display the histogram for (a) the LAPF, (b) the LMCPF with $\kappa = 1$, (c) the LMCPF with $\kappa = 2.5$ and (d) shows the LMCPF with $\kappa = 25$. The pink line displays the median, which is also shown on the top of each plot. Shown are the statistics for May 6th, 0 UTC.

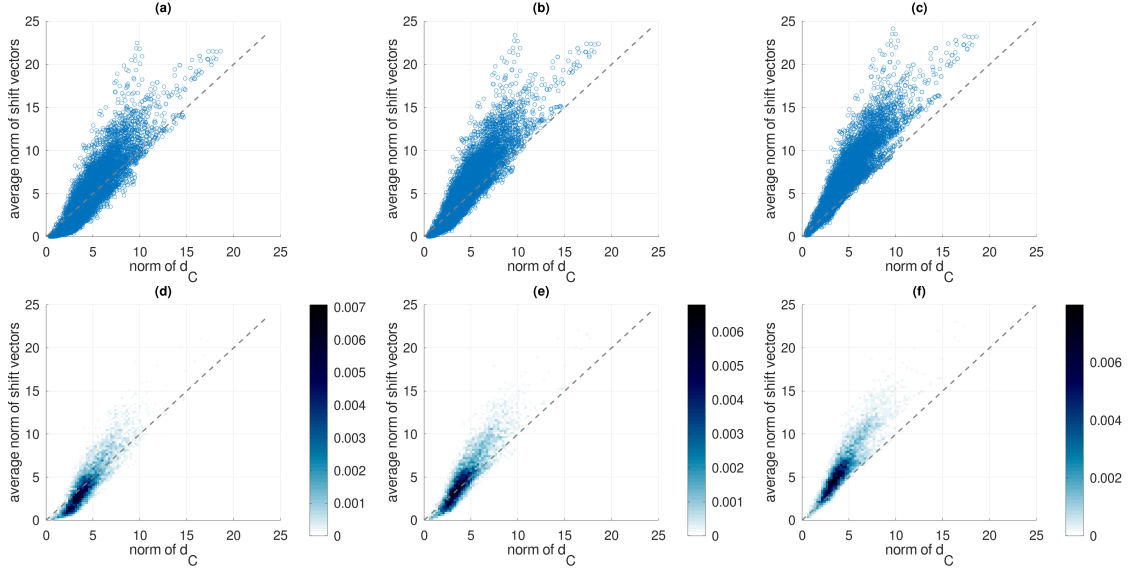


Figure 5: We show scatter and density plots of the average particle move versus the distance of the observation vector to the ensemble mean, all for the pressure level 500 hPa in ensemble space. On the x-axis we can see the norm of the observation distance to ensemble mean and on the y-axis we show the average size of the corresponding particle move. We display statistics for the LMCPF with different particle uncertainty, for each setting a scatter plot and a density plot which shows high density of points in a better way. (a) and (d) show the statistics for $\kappa = 1$, (b) and (e) for $\kappa = 2.5$ and (c) and (f) for $\kappa = 25$, all for May 6th, 0 UTC.

There are two effects seen in Figure 4. First, we see the distribution of average shifts or moves of the ensemble mean generated by the LAPF and the LMCPF with three different choices κ controlling the size of the uncertainty used for each particle. The mean shift increases if the uncertainty increases, i.e., from $\kappa = 1$ to $\kappa = 2.5$ and $\kappa = 25$. To develop an understanding of the relative size of this shift let us look at the one-dimensional version of formula (2.42) given by

$$s(\kappa) = \frac{\kappa b}{r + \kappa b}, \quad (4.6)$$

with background variance b and observation error variance r , reflecting the size of the particle move. When we, for example, choose $r = 4$ and $b = 16$, as we would get with typical values for the error of $2 \frac{m}{s}$ for wind measurements and an ensemble standard deviation of $4 \frac{m}{s}$, and then study $\kappa \in (1, 2.5, 10, 25)$, we obtain factors of size $s(\kappa) \in (0.8, 0.9, 0.97, 0.99)$. If the observation has a distance of 3.6 to the ensemble mean, as seen in Figure 2, this would make the means observed in Figure 4 plausible. For small $\kappa = 1$ here the particle move is 0.8 times the innovation, for large $\kappa = 25$ it is 0.99 times the innovation $y - H(x^{(b)})$. In Figure 4 we observe this behaviour with the median of the ensemble increments being $\text{median} = 2.62$ in (a) to $\text{median} = 3.54$ in (d).

As a final step of this part, we want to investigate not only the overall distribution of the particle moves, but relate the size of the average particle move to the distance of the observation to the ensemble mean. Figure 5 shows scatter and density plots for the LMCPF with different particle uncertainty. We employ the same values for κ as in Figure 4, (a) and (d) with $\kappa = 1$, (b) and (e) with $\kappa = 2.5$, (c) and (f) show results for $\kappa = 25$. Displayed are statistics for the average particle move vs. the difference of the observation vectors from the ensemble mean, all for the pressure level at 500 hPa.

The results of Figure 5 show that clearly the move of the particles is related to the necessary correction as given by the distance of the observation to the individual particle. There is a clear correlation of the average move to the observation discrepancy with respect to the ensemble mean. If we would investigate each particle individually in one dimension, all points would be on a straight line with slope given by (4.6). The situation in a high-dimensional space with non-homogeneous metric is more complicated as reflected by Figure 5. The figure confirms that the method is working as designed.

4.3 Assimilation Cycle Quality Assessment of the LMCPF

Here, studying standard global atmospheric scores for the analysis cycle we investigate the quality of the LMCPF by testing different choices of $\kappa > 0$, investigate the interaction effects between particle uncertainty, ensemble spread and

adaptive spread control and compare it to the way the LETKF moves the mean of the ensemble. For this aim we show two figures.

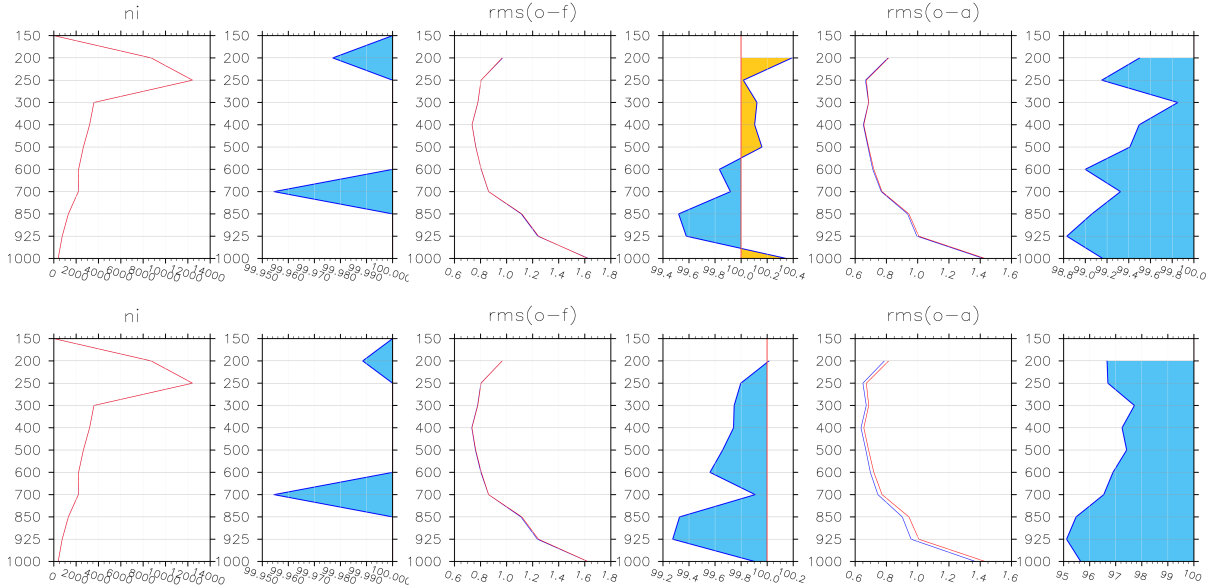


Figure 6: We show the observation verification of *upper air temperature* measured by airplanes, in particular the first guess and analysis scores. The three columns show the number of observations which passed quality control, the RMSE for $o - f$ statistics and the RMSE for $o - a$ statistics for two different choices of particle uncertainty. We display results for one global assimilation step at 20160506 03 UTC. In both cases the comparison of the LETKF (red line) with the LMCPF (blue line) is shown. In the first row we choose $\kappa = 1$, for the second row $\kappa = 2.5$

Figure 6 shows the functionality of the LMCPF by a display of the analysis and the first guess errors for upper air temperature for an ICON assimilation step, comparing the LETKF and the LMCPF with two different values of particle uncertainty controlled by γ or κ , respectively. Here, we show statistics for the LMCPF (blue line) with $\kappa = 1$ in row one and in row two we show the LMCPF (blue line) with $\kappa = 2.5$, both rows are showing the difference to the LETKF (red line). The left panel shows the number of observations which passed quality control, the middle panel shows the root mean square error (RMSE) of observation minus first guess statistics ($o - f$) (also known as observation - background ($o - b$) statistics) and the right panel shows the RMSE for observations minus analysis statistics ($o - a$). The blueish shading shows areas with lower values for the LMCPF in comparison to the LETKF.

It can clearly be seen that with respect to $o - f$ scores the LMCPF is able to outperform the LETKF in case studies with one assimilation step when an appropriate size of the uncertainty of each particle, here given by the size of κ , is found. In the large model error case we observe up to 5% improvement for the $o - a$ RMSE and 0.8% for the $o - f$ RMSE. These RMS errors for $o - a$ and $o - f$ are higher for the LMCPF with smaller particle uncertainty, but even the LMCPF with smaller particle uncertainty is able to outperform the LETKF in $o - f$ statistics for heights between 600 hPa and 925 hPa.

The numerical experiments prove that the particle uncertainty enables the LMCPF to move the background ensemble towards the observation in a way comparable to or even better than the LETKF. This effect remains active during model propagation and can also be observed for the first guess statistics and for forecasts with short lead times. Here, the LMCPF is able to outperform the operational version of the LETKF.

In Figure 7 we show a comparison of analysis cycle verification for a full one month period of LMCPF, LAPF and LETKF experiments. The columns are showing the same statistics as in Figure 6. The first row in Figure 7 shows the differences between LETKF (red line) and LMCPF with $\kappa = 2.5$ (blue line) for a full month of cycling. The second row shows the comparison of LAPF (red line) and LMCPF with $\kappa = 2.5$ (blue line) for the same period of time. Again, the blueish shading indicates lower numbers or RMSE values for the experiment (LMCPF), the yellowish shading indicates lower values for the reference (LETKF resp. LAPF).

Row one shows that the LMCPF with particle uncertainty given by $\kappa = 2.5$ can outperform the LETKF in regions below a height of 850 hPa and for short lead times – a very important region and time scale for practical applications. Here the LMCPF is up to 1.5% better than the LETKF for the $o - f$ statistics. In this experiment, for higher levels in

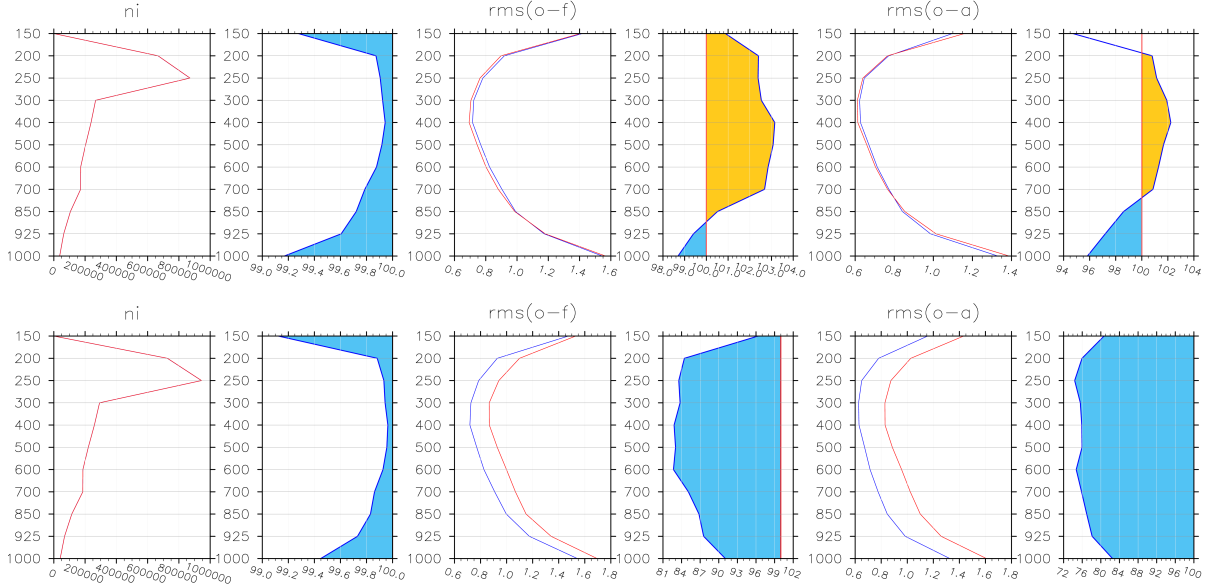


Figure 7: Again, we show some observation verification statistics for *upper air temperature* measured by airplanes. We show the same statistics as in Figure 6 but for three different experiments carried out for the period of May 2016. In the upper row the comparison between LETKF (red line) and LMCPF (blue line) is shown, in the lower row we show the comparison between LAMP (red line) and LMCPF (blue line).

the atmosphere the $o - a$ and $o - f$ statistics of the LMCPF are up to 3.5% worse than the LETKF. The amount of data which passes quality control is quite similar for all methods under consideration, however, at some levels we loose up to 0.9% of observations in comparison with the LETKF. This is an effect of quality control based on the ensemble spread - a smaller ensemble spread as we observe for the particle filter leads to less observations passing quality control. In the second row of Figure 7 we show the statistics of LAMP [Potthast et al., 2019] vs. LMCPF. Here we can clearly see that the LMCPF shows much better upper air scores than the LAMP. It clearly shows the importance to allow a movement of particles towards the observations by using particle uncertainty.

Overall we conclude that with respect to the verification of the analysis cycle the LMCPF with particle uncertainty given by $\kappa = 2.5$ is comparable to the LETKF, with some levels to be better, some to be worse, overall differences mostly below 3%. The upper air verification for the analysis cycle of the LMCPF in operational setup is more than 10% better than for the LAMP.

4.4 The Evolution of the Ensemble Spread

It is an important evaluation step to investigate the stability of the LMCPF for global NWP over longer periods of time. To this end, we have run a period of one month. We compare the particle spread evolution of the LMCPF, the LAMP and LETKF in Figure 8. All experiments were started with an ensemble which consists of 40 identical copies of the particles, i.e., with an ensemble in degenerate state. Thus, here the tests also evaluate the capability of the whole system to resolve degeneracy and return to an ensemble with reasonable stable spread.

In a sequence of experiments we have tested the ability of the LMCPF to reach and maintain a particular ensemble spread using a combination of the choice of κ with a posterior covariance inflation

$$\tilde{\mathbf{G}}_{ens}^{(a)} = \kappa_{post} \mathbf{G}_{ens}^{(a)} \quad (4.7)$$

for each particle with $\tilde{\mathbf{G}}_{ens}^{(a)}$ replacing $\mathbf{G}_{ens}^{(a)}$ in equation (2.49), which is used to generate the analysis ensemble by random draws. We also note that for the random draw of equation (2.47) we employed bounds given by c_0 and c_1 . The parameter combinations chosen for six different experiments over one week are compiled into Table 1. The corresponding spread evolution is visualized in Figure 8. The results show that, starting with an initial ensemble of identical particles, after some spin-up phase of 2-3 days all particle filters reach their particular spread level and keep it stable over a longer period of time. We carried out selected longer term studies comparing the behaviour of the LMCPF (red), the LAMP (blue) and the LETKF (black) over a period of one month.

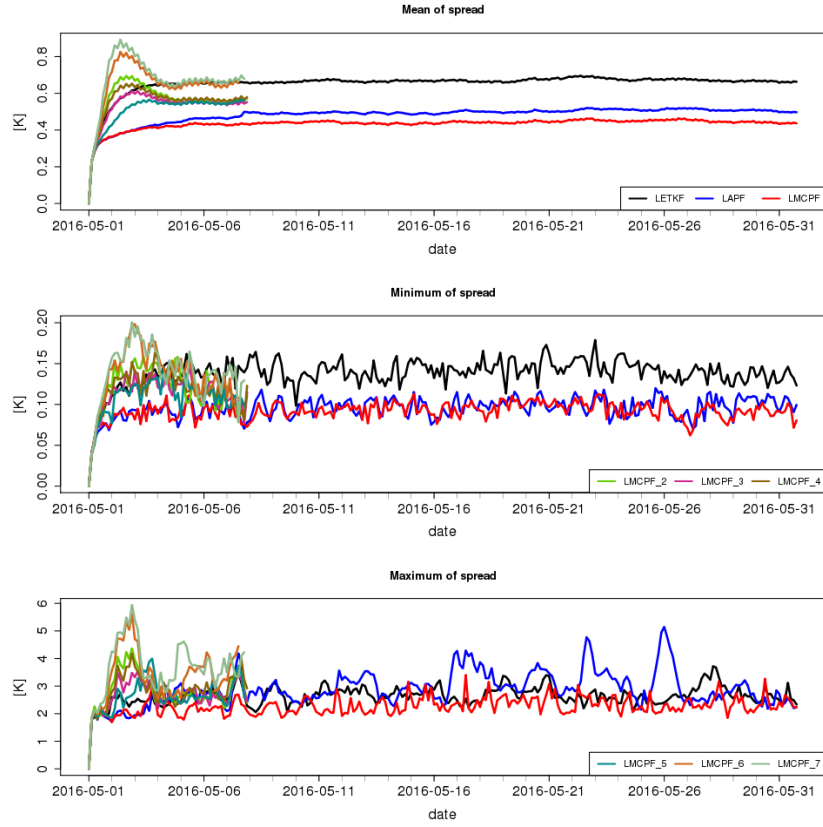


Figure 8: The evolution of the ensemble spread is shown for three filters and six different parameter choices for the LMCPF for a time period of both one month (LETKF - black, LAPF - blue, LMCPF - red) and for one week for different parameter choices for the LMCPF (see Table 1). The x-axis shows the period in one day steps. The y-axis shows the upper air temperature at ICON model level 64 (≈ 500 hPa) in Kelvin. The first row shows the mean of the spread, the second row the minimum and the third row the maximum.

Exp No.	κ	κ_{post}	c_1	$\rho^{(1)}$
2	0.5	5	0.5	1.5
3	0.5	3	0.5	1.5
4	0.3	5	0.5	1.5
5	1	1	0.3	3.0
6	0.5	3	0.5	3.0
7	0.3	5	0.5	3.0

Table 1: Parameter choices for the six one week experiments of Figure 8. Further, we used $c_0 = 0.02$ and $\rho^{(0)} = 1.0$ for all experiments.

The control of the ensemble spread is a delicate topic. A larger ensemble spread does not necessarily lead to better forecast scores, measured by RMSE (Skill) of the ensemble mean or its standard deviation (SD), defined as the RMSE after the bias has been subtracted. With the ability to control separately the strength of the adaptive resampling and the ability of the filter to pull the particles towards the observations, we have independent parameters at hand to adapt the approximations to a real-world situation. At the same time, the way the assimilation step of the LMCPF pulls the ensemble to the observations is based on both the size of the *particle uncertainty*, which itself is depending on the *ensemble spread*, and within the cycled environment on the adaptive resampling. Of course, it would be desirable to develop tools to estimate the real uncertainty adequate for each particle, and to keep all parts of the system consistent. We expect this to lead to much further research and discussions, which are beyond the scope of this work.

4.5 Forecast Quality of the LETKF and LMCPF Experiments

As the last part of the numerical results, we study the quality of longer *forecasts* based on the analysis cycle of the LMCPF with $\kappa = 2.5$ and compare it to the LETKF based forecasts in Figure 9 and to forecasts based on the LAPF analysis cycle in Figure 10. For this purpose, forecasts were run twice a day at 00 UTC and 12 UTC. In Figure 9 we display upper air verification for the LMCPF (dashed lines) and for the LETKF (solid lines). The different colors identify the different lead times, from one day up to one week. The first row shows the upper air temperature and the second row shows the u-component of wind. The first panel shows the Continuous Ranked Probability Score (CRPS), the second panel the Standard Deviation (SD), the third panel the Root Mean Square Error (RMSE) and the last panel shows the Mean (ME). For CRPS, SD and RMSE it is the aim to receive statistics as low as possible; for the Mean (=Bias) it is the goal to reach zero. We used the same observations for verification in both experiments.

Studying the results shown in Figure 9, we observe that the LMCPF shows slightly higher RMSE compared to the LETKF above 850 hPa. Forecast scores are nearly identical for LMCPF and LETKF for the upper air temperature, u-component of wind below 850hPa, i.e., where the first guess statistics have been better for LMCPF. For upper air temperature at low levels and for high lead times the LMCPF errors are smaller than those of the LETKF. For the u-component of wind up to a height of approx. 100 hPa the bias statistics of the LMCPF are better than the LETKF.

In Figure 10 we show the same statistics as in Figure 9 focussing on relative humidity and upper air temperature for the comparison of LMCPF and LAPF. Here, it can be clearly seen that the LMCPF shows lower RMS errors than the LAPF for both variables and for all levels. For relative humidity the LMCPF is clearly better for the shorter lead times up to three days, but with less prominence it still outperforms the LAPF for the longer lead times up to one week. For the upper air temperature the RMSE statistics are clearly better for the LMCPF for all lead times. It is worth noting that the biases for the two particle filters show a quite similar behaviour.

These results demonstrate that using particle uncertainty is an important ingredient for improving first guess and forecast scores of the particle filter.

5 Conclusions

In this work we develop the use of a Gaussian mixture within the framework of the Localized Adaptive Particle Filter (LAPF) introduced in Potthast et al. [2019], as an approximation to model and forecast particle uncertainty in the prior and posterior distributions. The filter, following earlier ideas of Hoteit et al. [2008] and Liu et al. [2016a,b] constructs an analysis distribution based on localized Gaussian mixtures, whose posterior coefficients, covariances and means are calculated based on the prior mixture given by the ensemble first guess and the observations. The analysis step is completed by resampling and rejuvenation based on the LAPF techniques, leading to a Localized Mixture Coefficients Particle Filter (LMCPF). In contrast to the LAPF the LMCPF is characterized by a move or shift of the first guess ensemble towards the observations, which is consistent with the non-Gaussian posterior distribution based on a Bayesian analysis step, and where the size of the move is controlled by the size of the uncertainty of individual particles.

We have implemented the LMCPF in the framework of the global ICON model for numerical weather prediction, operational at Deutscher Wetterdienst. Our reference system to test the feasibility of ideas and demonstrate the quality of the LMCPF is the LETKF implementation operational at DWD, which generates initial conditions for the global ICON Ensemble Prediction System ICON-EPS. We have shown that the LMCPF runs stably for a month of global assimilations in operational setup and for a wide range of specific LMCPF parameters. Our investigation includes a study of the distribution of observations with respect to the ensemble mean and statistics of the distance of ensemble members to the projection of the observations into ensemble space. We also study the average size of particle moves when uncertainty is employed for individual Gaussian particles within the LMCPF and provide an analytic explanation of the histogram shapes with a comparison to the eigenvalue distribution of the metrical tensors on which the particle weights are based.

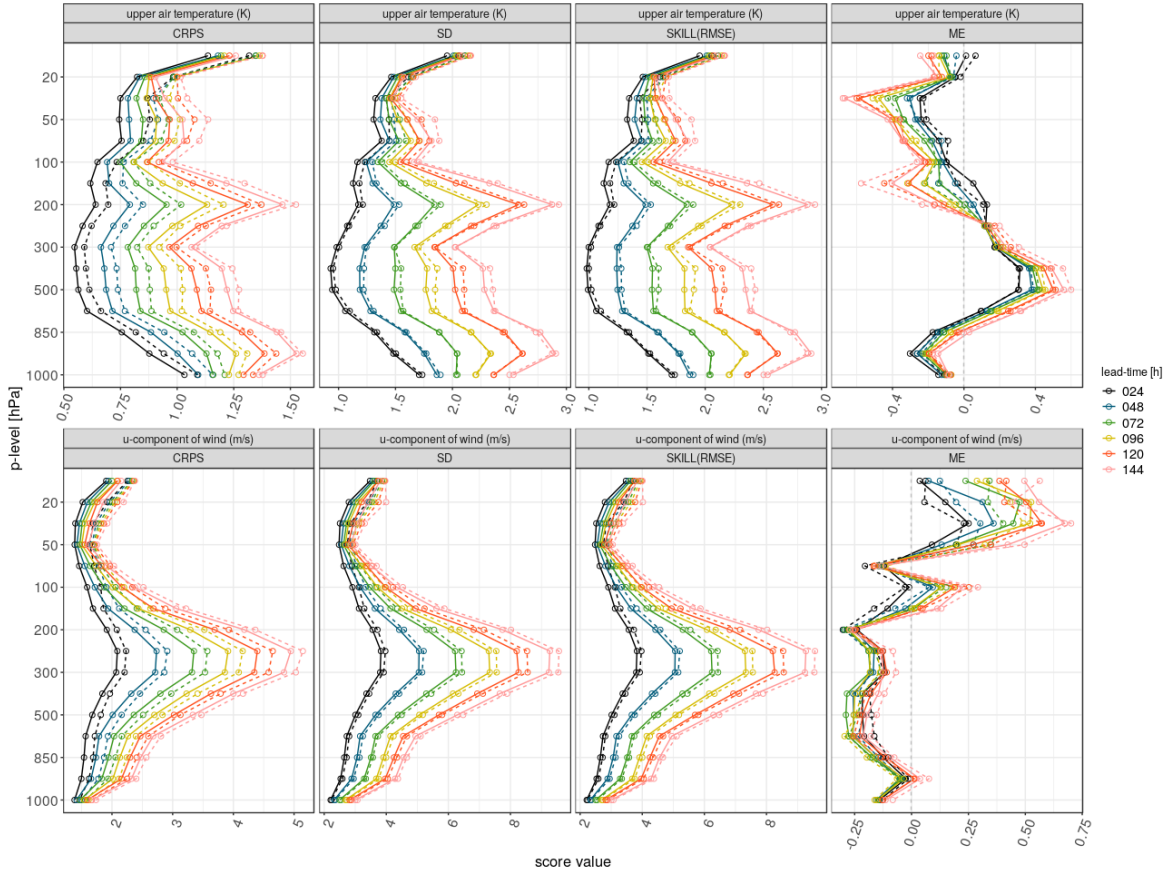


Figure 9: We display forecast scores for the LMCPF (dashed) and the LETKF (bold lines). Shown are the continuous rank probability score (CRPS), the standard deviation (SD), the RMSE and the mean (ME). First row shows the upper air temperature, the second row shows the u-component of wind measured by radiosondes. The colors indicate the different lead times from one day to 7 days.

We show that the upper air *first guess errors* of the LMCPF and LETKF during the assimilation cycle are very similar within a range of plus-minus 1-3%, with the LMCPF being better below 850 hPa and the LETKF being better above. *Forecast scores* for a time-period of one month have been calculated, demonstrating as well that the RMSE of the ensembles is comparable for upper air temperature and wind fields (2-3%). The size of the mean spread of the LMCPF strongly depends on parameter choices and is usually stable after a spin-up period.

In several shorter case studies we demonstrate that by varying the parameter choices, we can achieve better first guess RMSE for the LMCPF in comparison to the LETKF, which shows that for very short range forecasts the quality of the method can be comparable to or better than that of the LETKF. While reaching a break-even point for operational scores with a new method establishes an important mile-stone, we need to note that there are many open and intricate scientific questions here with respect to the choice of parameters for the Gaussian mixture and their inter-dependence as well as about the control of an optimal and correct ensemble spread both in the analysis cycle and for the forecasts.

Overall, with the LMCPF we demonstrate significant progress compared to the localized adaptive particle filter (LAPF) for numerical weather prediction in an operational setup, demonstrating that the LMCPF has reached a stability and quality comparable to that of the LETKF, while allowing and taking care of diverse non-Gaussian distributions in its analysis steps.

Clearly, there is much more work to be done. The automatic choice of current tuning parameters is an important topic. Also, in further steps we will take a look at the quality control. Currently, the LMCPF and the LETKF are using the same observation quality control, but the LMCPF seems to need a more accurate approach. Furthermore, we have implemented the LAPF and LMCPF in the Lorenz 63 and Lorenz 96 models and are studying the characteristics of the particle filters in low-dimensional systems.

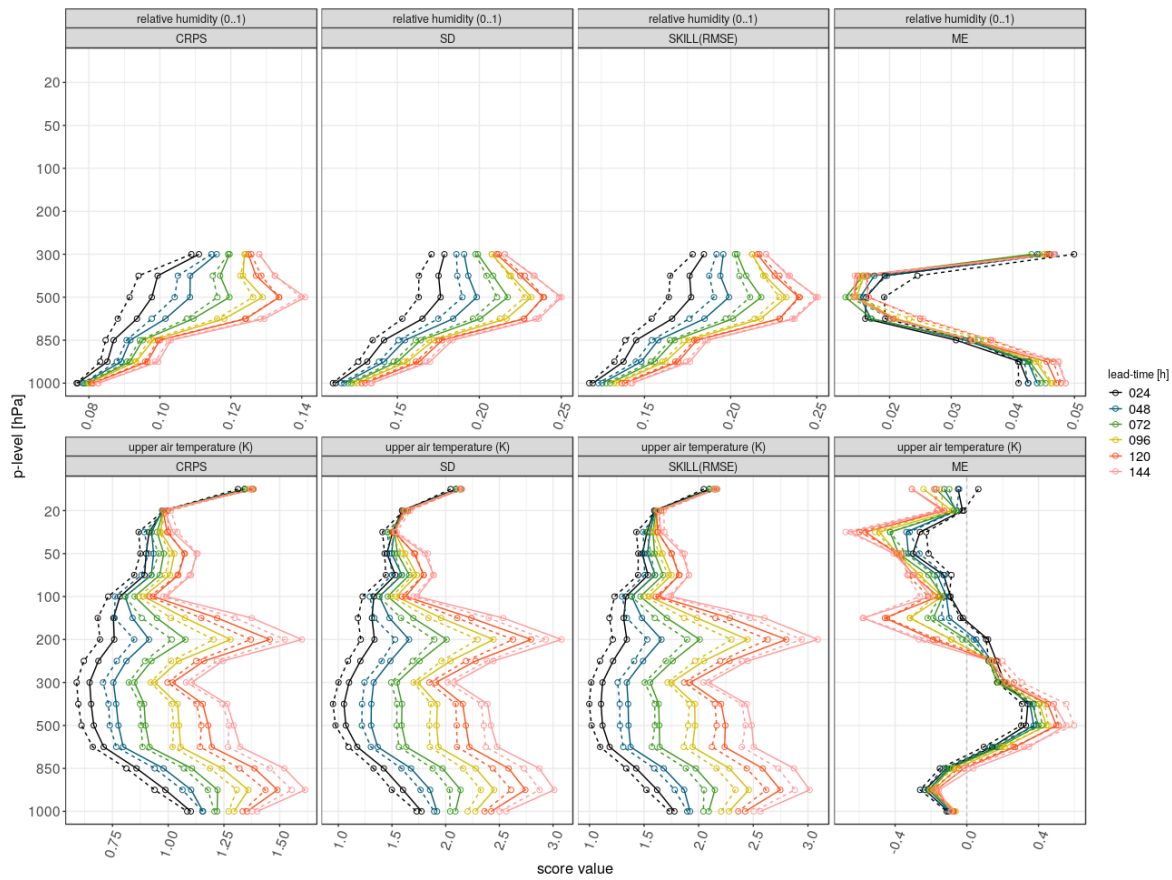


Figure 10: Similar to Figure 9, but for relative humidity and upper air temperature for LMCPF (dashed) and the LAPF (bold lines).

Acknowledgements

The research has been supported by the *Innovation in Applied Research and Development* (IAFE) grant of the German Ministry for Transport and Digital Infrastructure BMVI. The authors thank Dr. Harald Anlauf and Dr. Andreas Rhodin from DWD for much support working on the DACE data assimilation coding environment.

References

- Alan Bain and Dan Crisan. *Fundamentals of Stochastic Filtering*. Stochastic Modelling and Applied Probability. Springer, 2009. ISBN 978-0-387-76896-0. doi:10.1007/978-0-387-76896-0. URL <http://dx.doi.org/10.1007/978-0-387-76896-0>.
- Jeffrey L. Anderson and Stephen L. Anderson. A monte carlo implementation of the nonlinear filtering problem to produce ensemble assimilations and forecasts. *Monthly Weather Review*, 127(12):2741–2758, 1999. doi:10.1175/1520-0493(1999)127<2741:AMCIOT>2.0.CO;2. URL [https://doi.org/10.1175/1520-0493\(1999\)127<2741:AMCIOT>2.0.CO;2](https://doi.org/10.1175/1520-0493(1999)127<2741:AMCIOT>2.0.CO;2).
- Dan Crisan and Boris Rozovskii. *The Oxford Handbook of Nonlinear Filtering*. Oxford handbooks in mathematics. Oxford University Press, 2011. ISBN 9780199532902. URL <http://EconPapers.repec.org/RePEc:exp:obooks:9780199532902>.
- Peter Jan van Leeuwen. Nonlinear data assimilation in geosciences: an extremely efficient particle filter. *Quarterly Journal of the Royal Meteorological Society*, (136):1991–1999, 2010. doi:10.1002/qj.699.
- Chris Snyder, Thomas Bengtsson, Peter Bickel, and Jeff Anderson. Obstacles to high-dimensional particle filtering. *Monthly Weather Review*, 136:4629–4640, Dec 2008. doi:10.1175/2008MWR2529.1.

- Chris Snyder, Thomas Bengtsson, and Mathias Morzfeld. Performance bounds for particle filters using the optimal proposal. *Monthly Weather Review*, 143:4750–4761, Nov 2015. doi:10.1175/MWR-D-15-0144.1.
- Peter Bickel, Bo Li, and Thomas Bengtsson. *Sharp failure rates for the bootstrap particle filter in high dimensions*, volume 3 of *Pushing the Limits of Contemporary Statistics: Contributions in Honor of Jayanta K. Ghosh*, pages 318–329. Institute of Mathematical Statistics, Beachwood, Ohio, USA, 2008. doi:10.1214/074921708000000228. URL <https://doi.org/10.1214/074921708000000228>.
- Geir Evensen. Sequential data assimilation with a nonlinear quasi-geostrophic model using monte carlo methods to forecast error statistics. *Journal of Geophysical Research: Oceans*, 99(C5):10143–10162, 1994. ISSN 2156-2202. doi:10.1029/94JC00572. URL <http://dx.doi.org/10.1029/94JC00572>.
- Geir Evensen and Peter Jan van Leeuwen. An ensemble kalman smoother for nonlinear dynamics. *Monthly Weather Review*, 128:1852–1867, 2000. ISSN 60027-0644. doi:10.1175/1520-0493(2000)128<1852:AEKSFN>2.0.CO;2. URL [http://dx.doi.org/10.1175/1520-0493\(2000\)128<1852:AEKSFN>2.0.CO;2](http://dx.doi.org/10.1175/1520-0493(2000)128<1852:AEKSFN>2.0.CO;2).
- Geir Evensen. *Data Assimilation: The Ensemble Kalman Filter*. Earth and Environmental Science. Springer, 2009. ISBN 9783642037115. URL http://books.google.de/books?id=2_zatB_01AkC.
- Brian R Hunt, Eric J Kostelich, and Istvan Szunyogh. Efficient data assimilation for spatiotemporal chaos: A local ensemble transform Kalman filter. *Physica D: Nonlinear Phenomena*, 230(1-2):112–126, 2007. ISSN 0167-2789. doi:<http://dx.doi.org/10.1016/j.physd.2006.11.008>. URL <http://www.sciencedirect.com/science/article/pii/S0167278906004647>.
- Thomas Bengtsson, Chris Snyder, and Doug Nychka. Toward a nonlinear ensemble filter for high-dimensional systems. *Journal of Geophysical Research: Atmospheres*, 108(D24), 2003. doi:10.1029/2002JD002900. URL <https://agupubs.onlinelibrary.wiley.com/doi/abs/10.1029/2002JD002900>.
- Craig H Bishop. The GIGG-EnKF: ensemble kalman filtering for highly skewed non-negative uncertainty distributions. *Quarterly Journal of the Royal Meteorological Society*, 142(696):1395–1412, 2016. doi:10.1002/qj.2742. URL <https://rmets.onlinelibrary.wiley.com/doi/abs/10.1002/qj.2742>.
- Sanita Vetra-Carvalho, Peter Jan van Leeuwen, Lars Nerger, Alexander Barth, M. Umer Altaf, Pierre Brousseau, Paul Kirchgeßner, and Jean-Marie Beckers. State-of-the-art stochastic data assimilation methods for high-dimensional non-gaussian problems. *Tellus A: Dynamic Meteorology and Oceanography*, 70(1):1–43, 2018. doi:10.1080/16000870.2018.1445364.
- Peter Jan van Leeuwen, Hans R. Künsch, Lars Nerger, Roland Potthast, and Sebastian Reich. Particle filters for high-dimensional geoscience applications: A review. *Quarterly Journal of the Royal Meteorological Society*, 145(723):2335–2365, 2019. doi:10.1002/qj.3551. URL <https://rmets.onlinelibrary.wiley.com/doi/abs/10.1002/qj.3551>.
- E Klinker, Florence Rabier, G Kelly, and Jean-François Mahfouf. The ecmwf operational implementation of four-dimensional variational assimilation. iii: Experimental results and diagnostics with operational configuration. *Quarterly Journal of the Royal Meteorological Society*, 126:1191–1215, 2000. doi:10.1002/qj.49712656417. URL <http://dx.doi.org/10.1002/qj.49712656417>.
- Peter Jan van Leeuwen. Particle filtering in geophysical systems. *Monthly Weather Review*, 137(12):4089–4114, 2009. doi:10.1175/2009MWR2835.1.
- Peter Jan van Leeuwen, Yuan Cheng, and Sebastian Reich. *Nonlinear Data Assimilation*. Frontiers in Applied Dynamical Systems: Reviews and Tutorials. Springer, 2015. ISBN 978-3-319-18347-3. doi:10.1007/978-3-319-18347-3. URL <http://dx.doi.org/10.1007/978-3-319-18347-3>.
- Alban Farchi and Marc Bocquet. Comparison of local particle filters and new implementations. *Nonlinear Processes in Geophysics*, 25:765–807, 2018. doi:10.5194/npg-25-765-2018. URL <https://doi.org/10.5194/npg-25-765-2018>.
- Sebastian Reich and Colin Cotter. *Probabilistic Forecasting and Bayesian Data Assimilation*. Cambridge University Press, 2015. ISBN 9781107706804. doi:10.1017/CBO9781107706804. URL <https://doi.org/10.1017/CBO9781107706804>.
- Jonathan Poterjoy and Jeffrey L. Anderson. Efficient assimilation of simulated observations in a high-dimensional geophysical system using a localized particle filter. *Monthly Weather Review*, (144):2007–2020, 2016. doi:10.1175/MWR-D-15-0322.1.
- Stephen G. Penny and Takemasa Miyoshi. A local particle filter for high-dimensional geophysical systems. *Nonlinear Processes in Geophysics*, 23:391–405, 2016. doi:10.5194/npg-23-391-2016. URL www.nonlin-processes-geophys.net/23/391/2016/doi:10.5194/npg-23-391-2016.

- Roland Potthast, Anne Walter, and Andreas Rhodin. A localized adaptive particle filter within an operational nwp framework. *Monthly Weather Review*, 147(1):345–362, 2019. doi:10.1175/MWR-D-18-0028.1.
- Takuya Kawabata and Genta Ueno. Non-gaussian probability densities of convection initiation and development investigated using a particle filter with a storm-scale numerical weather prediction model. *Monthly Weather Review*, 148:3–20, January 2020. doi:10.1175/MWR-D-18-0367.1.
- Jonathan Poterjoy, Ryan A. Sobash, and Jeffrey L. Convective-scale data assimilation for the weather research forecasting model using the local particle filter. *Monthly Weather Review*, 145:1897–1918, 2017. doi:10.1175/MWR-D-16-0298.1.
- M. Frei and H.R. Künsch. Bridging the ensemble kalman and particle filters. *Biometrika*, 100(4):781–800, 2013. doi:10.1093/biomet/ast020. URL <https://doi.org/10.1093/biomet/ast020>.
- Sylvain Robert, Daniel Leuenberger, and Hans Rudi Künsch. A local ensemble transform Kalman particle filter for convective-scale data assimilation. *Quarterly Journal of the Royal Meteorological Society*, 2017. ISSN 1477-870X. doi:10.1002/qj.3116. URL <http://dx.doi.org/10.1002/qj.3116>.
- I. Hoteit, D.-T. Pham, G. Triantafyllou, and G Korres. A new approximate solution of the optimal nonlinear filter for data assimilation in meteorology and oceanography. *Monthly Weather Review*, 136:317–334, 2008. doi:10.1175/2007MWR1927.1.
- Bo Liu, Boujemaa Ait-El-Fquih, and Ibrahim Hoteit. Efficient kernel-based ensemble gaussian mixture filtering. *Monthly Weather Review*, 144(2):781–800, 2016a. doi:10.1175/MWR-D-14-00292.1.
- Bo Liu, M. E. Gharamti, and Ibrahim Hoteit. Assessing clustering strategies for gaussian mixture filtering a subsurface contaminant model. *Journal of Hydrology*, 535:1–21, 2016b. doi:10.1016/j.jhydrol.2016.01.048.
- Gen Nakamura and Roland Potthast. *Inverse Modeling*. 2053-2563. IOP Publishing, 2015. ISBN 978-0-7503-1218-9. doi:10.1088/978-0-7503-1218-9. URL <http://dx.doi.org/10.1088/978-0-7503-1218-9>.
- Günther Zängl, Daniel Reinert, Pilar Rípodas, and Michael Baldauf. The icon (icosahedral non-hydrostatic) modelling framework of dwd and mpi-m: Description of the non-hydrostatic dynamical core. *Quarterly Journal of the Meteorological Society*, (141):563–579, March 2014. doi:10.1002/qj.2378.